

SI NANORODS ENHANCED ANISOTROPIC WETTING ON COMPACT DISK SURFACE

By

JUN CHEN

(Under the Direction of Yiping Zhao)

ABSTRACT

Engineering and controlling surface anisotropic wettability and liquid spreading on patterned surfaces is an active area of research, which is of significant interest for a broad range of applications. Here, we report that nano-microstructured hybrid thin films, composed of an array of Si nanorods growing onto the compact disk Surface by means of oblique angle deposition, demonstrate a significantly enhanced anisotropic wetting behavior. The surface wetting anisotropy is characterized by the increase of the watermark aspect ratio from 1.17 to 4.57. Furthermore, resort to HFTS treatment, an anisotropic wetting study on the compact disk surface was carried out from both hydrophobic and hydrophilic perspectives. Both the hydrophilic and hydrophobic anisotropic wettings are interpreted by the Cassie's law and Wenzel's law. And coupled with a qualitative interpretation in a thermodynamic view, our models fittingly describe the nanostructure's anisotropic wetting behavior as functions of measureable surface morphology parameters.

INDEX WORDS: Oblique angle deposition, Contact angle, Anisotropic wetting, Silicon nanorod, Compact Disk, Patterned surface, HFTS, Superhydrophobic, Matlab.

SI NANORODS ENHANCED ANISOTROPIC WETTING ON COMPACT DISK SURFACE

By

JUN CHEN

B.E., Huazhong University of Science and Technology, China, 2007

A Thesis Submitted to the Graduate Faculty of The University of Georgia in Partial Fulfillment
of the Requirements for the Degree

MASTER OF SCIENCE

ATHENS, GEORGIA

2012

© 2012

JUN CHEN

All Rights Reserved

SI NANORODS ENHANCED ANISOTROPIC WETTING ON COMPACT DISK SURFACE

By

JUN CHEN

Major Professor: Yiping Zhao

Committee: Ernest W. Tollner

Jianguo Fan

Electronic Version Approved:

Maureen Grasso
Dean of the Graduate School
The University of Georgia
May 2012

ACKNOWLEDGEMENTS

This thesis would not have been completed without the efforts of a few key individuals, to whom I cannot express enough gratitude.

First and foremost, my sincere thanks go to my major advisor Dr. Yiping Zhao for his mentoring, tutoring and financial supporting me in the past two years. Dr. Zhao has been very generous with his time and wisdom. His attitude towards life and scientific research really inspired me a lot. The research work under his guidance in The University of Georgia will be a valuable and beneficial experience in my life.

Besides, I also would love to show my sincere thanks to Dr. Ernest W. Tollner. As a graduate coordinator, he helped me a lot with great kind and patience. As one of my committee members, he also gave me insightful guidance and advices. Especially, he led me to get a better understanding of the surface tension in an energy view, which is a very critical thinking in the area of anisotropic wetting study.

Furthermore, I would also love to give my special thanks to Dr. Jianguo Fan for his support and guidance in my graduate study in UGA. As one of my committee members, he helped me not only academically, but also mentally. Just like my older brother, his great kind as well as encouragement accompanied and led me through a lot of depressions and frustrations in my life. I really appreciate his great help and meticulous instructions when I study in UGA in the past two years. And I will be grateful and always appreciate it in the rest of my life.

In addition, I could not go without acknowledging my lab-mates, specifically including Yuping He, Jing Chen, Justin Abell, Monaj Manjare, George Larson, Hao Zhu, Yue Zhao, Yizhuo He, Kun Yao and so on. They are an integral part to this thesis research, tremendously helpful, pragmatic and supportive.

Last but not least, sincere thanks to my families for their everlasting support. And also all of my friends, especially including Dr. M. Howard Lee, Dr. William Kisaalita, Christopher William Oliver, Zhigang Tao, Chunyuan Song, Ping Zhang, Haidong Yang, Jianbiao Tang, Xuewei Qi, Wei Cao, Qiongge Li, Qin Huang, Yifei Wu, Rui Cheng. A great deal of credits are owed to their support and encouragement in developing this technical report.

TABLE OF CONTENTS

	Page
ACKNOWLEDGEMENT.....	IV
LIST OF TABLES.....	VIII
LIST OF FIGURES.....	IX
CHAPTER	
1 INTRODUCTION.....	1
1.1 Fundamental Concepts in Wetting	3
1.2 Oblique Angle Deposition	10
1.3 Current Status of Research in Anisotropic Wetting Study.....	13
1.4 Motivation of This Research.....	19
1.5 Organization of the Thesis.....	20
2 EXPERIMENTAL DESIGN AND PREPARATION.....	21
2.1 Substrate Preparation.....	21
2.2 Sample Fabrication.....	22
2.3 SEM and AFM Characterization.....	24
2.4 Chemical Treatment.....	24
2.5 Sessile Droplet Method.....	26
2.6 Sliding angle Measurement.....	27
2.7 Watermark and Droplet Shape Photography.....	28

3	HYDROPHILIC ANISOTROPIC WETTING.....	30
	3.1 Experimental Results.....	30
	3.2 Data Interpretation and Discussion.....	35
	3.3 Conclusion.....	44
4	HYDROPHOBIC ANISOTROPIC WETTING.....	45
	4.1 Experimental Results.....	45
	4.2 Data Interpretation and Discussion.....	45
	4.3 Conclusion.....	51
5	CONCLUSION AND FUTURE WORK.....	53
	REFERENCES.....	55
	APPENDICES.....	65
A	THE CALCULATION OF ARBITRARY ARC LENGTH ALONG A COSINE FUNCTION.....	65
B	FREE ENERGY AND FREE ENERGY BARRIER DISTRIBUTION ON GROOVED SURFACE.....	67
C	SLIDING ANGLE QUALITATIVE ANALYSIS IN A THERMODYNAMIC VIEW.....	74

LIST OF TABLES

	Pages
Table 3.1: Static Contact Angle Measurement on Si Thin Film Modified Surface.....	32
Table 3.2: Static Contact Angle Measurement on SiNR Modified Surface.....	32
Table 3.3: Water Droplet on Si Thin Film Modified Samples.....	33
Table 3.4: Watermark on SiNR Modified Samples.....	34
Table 4.1: Static Contact Angle Measurement on Si thin film modified surface with HFTS Treatment.....	46
Table 4.2: Static Contact Angle Measurement on SiNR Modified Surface after HFTS Treatment.....	46
Table 4.3: Sliding Angle Measurement for SiNR Modified Samples.....	51

LIST OF FIGURES

	Page
Figure 1.1: A sketch of designed apparatus for the water surface tension estimation.....	3
Figure 1.2. A sketch of the contact angle and the forces acting on a three phase contact line.....	5
Figure 1.3. The classification of different wetting of solid surfaces by a liquid drop.....	5
Figure 1.4. The infinitesimal displacement of the three phase contact line on a rough solid surface (move towards the left).....	7
Figure 1.5. The infinitesimal displacement of the three phase contact line on a flat and smooth, but chemically heterogeneous solid surface (move towards the left).....	8
Figure 1.6. A sketch of water resting on a porous solid surface. (a) Water droplet in a Cassie's state. (b) Water droplet in a Wenzel's state.....	9
Figure 1.7. Sliding angle captured by tilting base method.....	10
Figure 1.8. Nucleation and shadowing growth. (a) Adatoms condense and nucleation. (b) column growth as results of shadowing of the initial nuclei and column will grow oriented towards the direction of incident vapor.....	11
Figure 1.9. SEM images of several nanostructures fabricated by OAD. (a) Ag nanorods array with a length of $\sim 1 \mu\text{m}$ was deposited using the OAD technique at vapor incident	

angle of 86° . (b) Si nanorods array with QCM reading 2000nm was deposited by OAD technique on Compact Disk surface at a vapor incident angle of 86° . (c) Si nanorods array with QCM reading 2000nm was deposited by OAD technique with substrate rotation at 0.5 rev/s on Si wafer at a vapor incident angle of 86° . (d) Si nanorods array with QCM reading 2000nm was deposited by GLAD technique with substrate rotation at 0.5 rev/s on Compact Disk surface at a vapor incident angle of 86°12

Figure 1.10. The schematic anisotropic liquid droplet top view representation.....13

Figure 2.1. Substrates arrangement for oblique angle deposition. (a) A sketch shown cutting the CD. (b) The substrate arrangement on a substrate holder.....22

Figure 2.2. Custom-designed electron beam-sputtering evaporation system for OAD. (a) A sketch of the setup for template oblique angle deposition. (b) Photograph of electron beam-sputtering evaporation system in our lab for OAD.....23

Figure 2.3. Molecular structure of HFTS.....24

Figure 2.4. (a) The CVSM setup for HFTS SAM creation. (b) Photograph of the CVSM setup in our lab.....25

Figure 2.5. Static contact angle (CA) measurement on the samples before or after HFTS treatment. (a-b) Static contact angle measurement on silicon wafer. Before HFTS treatment: CA= 28.5° . After HFTS treatment, CA= 113.9° . (c-d) Static contact angle measurement on glass wafer. Before HFTS treatment: CA= 27.2° . After HFTS treatment, CA= 113.5° .(e-f) Static contact angle measurement on QCM reading 1000nm Si Nanorods, fabricated with GLAD technique with rotation speed 0.005

rev/s at 86° vapor incident angle. Before HFTS treatment: $CA=3.2^\circ$. After HFTS treatment, $CA=155.6^\circ$	26
Figure 2.6. The contact angle measurement system (Data Physics OCA 20) in our lab: a liquid droplet (DI water for all my experiments) is deposited onto the samples' surface through a microsyringe, the contour the liquid droplet is captured by a CCD camera.....	27
Figure 2.7. A custom built system for sliding angle measurement.....	28
Figure 2.8. Phantom digital high speed image system for photography of the water droplet resting on the samples in a millimeter scale.....	29
Figure 3.1. Anisotropic droplet quantitative analysis: (a) schematic water droplet top-view representation and (b) photograph of an asymmetric DI water droplet on a polymer-stripped-off CD surface with an aspect ratio of 1.17, which is defined by the ratio of its length to width, where length L is the size of the watermark along the surface grooves and the width W is the size of the watermark perpendicular to the surface grooves. (c-d) The water droplet profile and static contact angle measurement demonstration.....	31
Figure 3.2. A sketch for the Hemi-wicking. The water film propagates from a deposited drop, a small amount of liquid is sucked into the tilted silicon nanorods, and then spread across the water-silicon composite to form the equilibrium contact angle.....	35
Figure 3.3. An AFM characterization of the polymer-stripped-off CD surface. (a) Top view of $10 \times 10 \mu\text{m}^2$ topographic image and (b) 3D view of the $25 \times 25 \mu\text{m}^2$ topographic image.....	37
Figure 3.4. A mathematic description of the polymer-stripped-off CD surface profile, based on	

the measured surface parameters by Atomic force microscopy (AFM, Veeco Metrology Group).....	37
Figure 3.5. SEM image of SiNR on the CD surface with vertical growth. (a) Top view. (b-c) Oblique view. (d) Cross section view.....	39
Figure 3.6. The model of the surface profile of SiNR on CD substrate with vertical growth.....	40
Figure 3.7. A rough sketch of surface morphology comparison for SiNR growing. (a) ⊥ surface grooves and (b) surface grooves.....	41
Figure 3.8. A morphological model of SiNR on CD substrate with parallel growth.....	42
Figure.4.1. A sketch of water droplet resting on hydrophobic silicon nanorod surfaces.....	45
Figure 4.2. An AFM characterization of the polymer-stripped-off CD surface. Top view of 10× 10 μm ² topographic image and also its corresponding section analysis data. The AFM pictures analysis is carried out with the Nanoscope Control Software (Quadrex, Digital Instrument).....	48
Figure 4.3. A sketch of the cross-sectional view of the water droplet resting on the sample of the SiNR vertical growth on CD substrate in a Cassie's state.....	49
Figure 4.4 A sketch of the cross-sectional view of the water droplet resting on the sample of the SiNR parallel growth on CD substrate in a Cassie's state.....	50

CHAPTER 1

INTRODUCTION

In nature, anisotropic textured surfaces have direction-dependent physical and chemical properties that provide the basis for diverse functionalities such as superior adhesion for geckos (Huber et al, 2005), locomotion for water strider (Bush et al, 2007), water repellence of butterfly wings (Zheng et al, 2007), pollination for plants (Oelschlägel et al, 2009), and droplet propelling for shorebirds beaks (Prakash et al, 2008). By mimicking the natural textures and engineering synthetic materials to control surface anisotropic wettability is of significant interests for a broad range of applications, including digital microfluidic devices (Extrand et al, 2007; Berthier et al, 2008), drug delivery (Pesika et al, 2009; Mahdavi et al, 2008), DNA microarrays (Chiou et al, 2007), digital lab-on-a-chip devices (Wang et al, 1997), anti-fogging and fog-harvesting (Krupenkin et al, 2004; Cebeci et al, 2006; Garrod et al, 2007), inkjet printing (Wang et al, 2004;) and thin-film lubrication (Hiratsuka et al, 2007; Extrand et al, 2007), etc.

Recently, advancements in surface engineering, with the fabrication of various micro/nanoscale topographic features (Bico et al, 1999; Oner et al, 2000; Yoshimitsu, et al. 2002; Quéré et al, 2005; Seemann et al, 2005; Maritines et al, 2005) and selective chemical patterning on surfaces (Gleiche et al, 2000; Zhao et al. 2001; Dupuis et al, 2005), have been used to enhance surface anisotropic wettability (Wenzel et al, 2000; Vorobyev and Guo, 2009), and enable the control of the liquid of the film thickness (Xiao et al, 2009) and the shape of final wetted area (Courbin et al, 2007).

Experimentally, surface groove geometries and chemically patterned inhomogeneous surfaces can produce anisotropic wetting, which results in contact angle variations in different directions and elongated droplet shapes (Drelich et al, 1996; Gau et al, 1999; Bico et al, 1999; Chen et al, 2005; Chung et al, 2007; Zhang et al, 2007; Kusumaatmaja et al, 2008). Drelich (1996) have prepared micrometer-sized heterogeneous surfaces consisting of alternating and parallel hydrophobic/hydrophilic strips by microcontact printing using an elastomer stamp. Morita (2005) has also obtained micrometer-scale patterned fluoroalkylsilane monolayer surfaces with liquidphobic/liquidphilic strips by vacuum ultraviolet (VUV) photolithography. However, they failed to fabricate a wide area patterned surface with a $< 1\mu\text{m}$ line width to evaluate the wetting anisotropy. Gleiche (2000 and 2001) has fabricated submicrometer-scale patterned surface consisting of stripes and channels with alternating wettability using wetting instabilities during the Langmuir-Blodgett film transfer, and demonstrated anisotropic wetting properties on those substrates. Although anisotropic wetting on geometrical structures has been studied using micrometer-scale features (Chen, et al. 2005), due to technical limitations, there has been no deliberate effort to demonstrate whether submicrometric, or smaller features would also lead to the macroscopic distortion of water drops or anisotropic wetting.

In this thesis, we propose to use Si nanorod arrays fabricated by a so-called oblique angle deposition method to significantly enhance the anisotropic wetting of compact disk groove surfaces. This simple and effective method can provide a general approach to enhance the surface wetting anisotropy of any grooved surfaces. The resulted hydrophilic and hydrophobic surfaces are analyzed by sessile droplet method measurements as well as sliding angle characterization. A quantitatively analysis *via* Cassie's Law and Wenzel's Law is applied to

describe the nanostructure's anisotropic wetting behaviors as a function of measurable surface morphology parameters.

1.1 Fundamental Concepts in Wetting

1.1.1 Surface Tension

The surface tension γ of a liquid is the magnitude of the force F exerted parallel to the surface of a liquid divided by a line of length L over which the force acts, which has a unit of N/m. The surface tension is an increased attraction of molecules at the surface of a liquid resulting from forces of attraction on the sides with fewer liquid molecules.

With some iron wires or glass rods, we can make a three-sides rectangle and a slider, as it is indicated in Fig. 1.1. And then dip this apparatus into to the DI water. As soon as the apparatus is removed from the liquid, one observes that the mobile rod moves spontaneously in the direction of the surface tension force so as to decrease the surface area of the liquid.

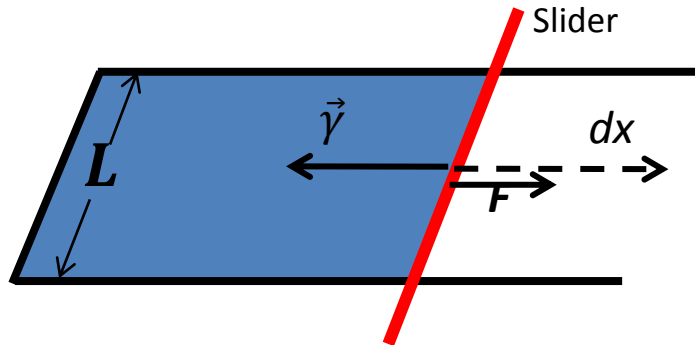


Figure 1.1. A sketch of designed apparatus for the water surface tension estimation.

Here, a water surface can be treated as a stretched membrane characterized by a surface tension that opposes its distortion, in order to minimize its surface energy. If the mobile slider moves by a distance Δx , the work done by the surface tension is:

$$\Delta W = F \cdot \Delta x = \gamma \cdot L \cdot \Delta x. \quad (1.1)$$

This demonstrates that γ is also the force exerted per unit length of the rod. In conclusion, γ is a force (per unit length) normal to the rod in the plane of the surface and directed toward the liquid.

Technically, surface tension, which has the dimension of force per unit length, or of energy per unit area. For a liquid, the surface tension (force per unit length) and the surface energy density are identical. But when referring to energy per unit of area, one should use the term surface energy—which is a more general term in the sense that it applies not only to liquids, but also to solids. Water has a surface energy density of 0.072 J/m^2 and a surface tension of 0.072 N/m .

1.1.2 Contact Angle of an Ideal Solids Surface

When a droplet of liquid spreading on a flat solid surface, it will form a spherical cap. And the contact angle is an angle at which the liquid/vapor interface meets the solid surface, as shown in Fig. 1.2. The contact angle θ is the result of the three-phase interaction (vapor, liquid and solid) measured at the contact line. Fig. 1.2 is a sketch showing the forces acting on the three-phase contact line. At equilibrium, the force balance in the horizontal direction can be written as:

$$\gamma_{lv} \cdot \cos \theta = \gamma_{sv} - \gamma_{sl}, \quad (1.2)$$

$$\text{or} \quad \cos \theta = \frac{\gamma_{sv} - \gamma_{sl}}{\gamma_{lv}}, \quad (1.3)$$

where γ_{sv} , γ_{sl} and γ_{lv} designate the surface tensions between phase solid and vapor, solid and liquid, liquid and vapor, respectively. Eq. (1.2) and (1.3) was first derived by Thomas Young (Young, 1805).

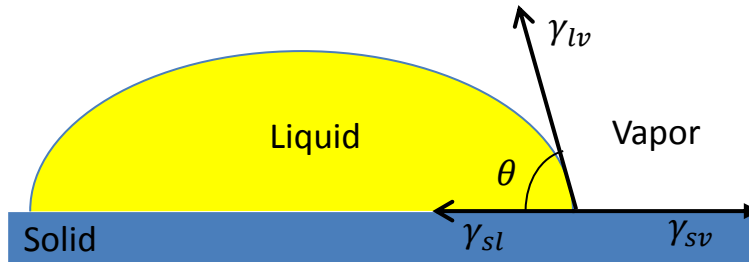


Figure 1.2. A sketch of the contact angle and the forces acting on a three phase contact line.

Based on the Young's Model, when a liquid is deposited onto a solid surface, the liquid droplet will spread, driven by the solid/vapor surface tension, and balanced by the reaction forces from the liquid/vapor and solid/liquid tensions.

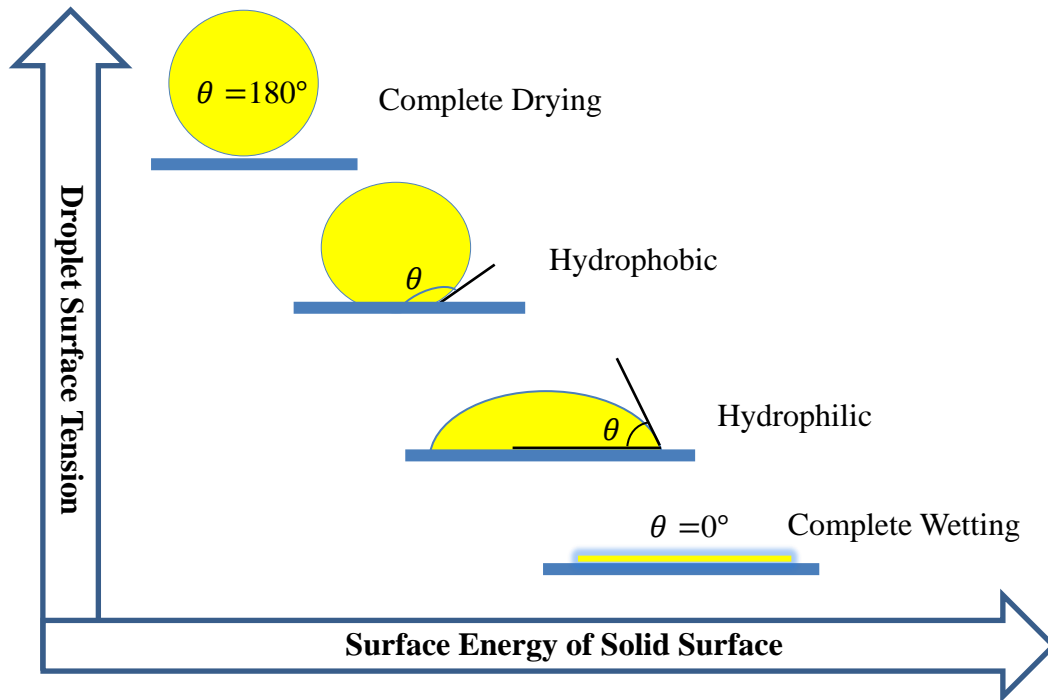


Figure 1.3. The classification of different wetting of solid surface by a liquid drop.

The contact angle provides valuable information on the properties of the material surface, including, adhesion, wettability, solid surface free energy, and surface cleanliness. According to the value of the contact angle θ , in general, all surfaces can be classified in to two categories:

hydrophilic surface if $\theta < 90^\circ$ and hydrophobic surface if $90^\circ < \theta < 180^\circ$. For hydrophilic surface, when contact angle $\theta = 0^\circ$, it is called complete wetting. And for hydrophobic surface, when contact angle $\theta = 180^\circ$, it is called complete drying. Fig. 1.3 shows the classification of different wetting of solid surfaces.

1.1.3 Apparent Contact Angle of a Rough Surface

Real surfaces are rarely ideal, *i.e.* perfectly flat and chemically homogenous. They are usually either physically rough or chemically heterogeneous, or both. Both the surface roughness and chemical heterogeneity can dramatically affect the surface apparent contact angles.

R.N. Wenzel was the first to consider the influence of roughness on contact angle, and derived the Wenzel's Model (Wenzel, 1936). He considered a rough and chemically homogeneous surface, as shown in Fig. 1.4. The surface energy change due to the infinitesimal displacement of the three phase contact line on a rough solid surface shown in Fig.1.4 can be written as,

$$dE = r \cdot (\gamma_{sl} - \gamma_{sv}) \cdot dx + \gamma_{lv} \cdot dx \cdot \cos \theta^*, \quad (1.4)$$

where r is the roughness factor of the rough surface, which is defined as the ratio of the real surface area to the projected surface area, and $r \geq 1$. θ^* is the apparent contact angle. For $r = 1$ (flat surface), we can recover Young's Equation. When $dE=0$, we obtain the expression for θ^* ,

$$\cos \theta^* = r \cdot \cos \theta, \quad (1.5)$$

where θ is the Young's angle.

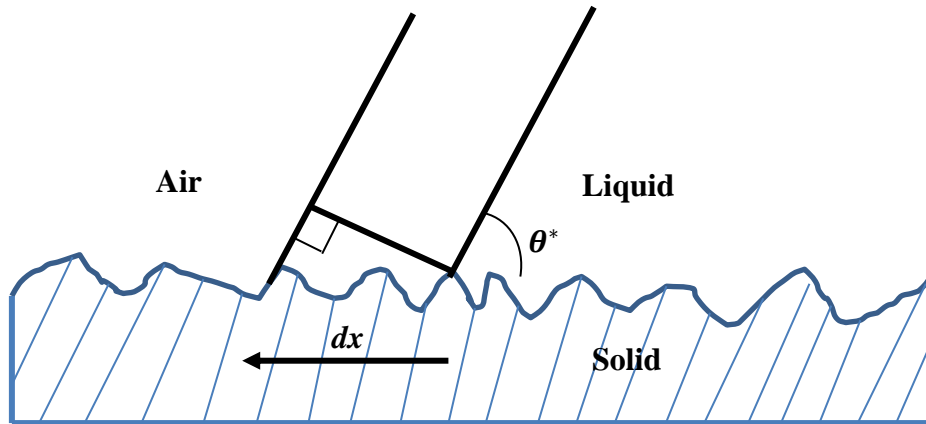


Figure 1.4. The infinitesimal displacement of the three phase contact line on a rough solid surface (move towards the left).

From the Eq. 1.5, we can draw two conclusions:

1. For a hydrophilic surface with $\theta < 90^\circ$, surface roughness will make the surface more hydrophilic, i.e., $\theta^* < \theta$.
2. For a hydrophobic surface with $\theta > 90^\circ$, the surface roughness will make the surface more hydrophobic, i.e., $\theta^* > \theta$.

However, the roughness factor r could be intentionally made to be arbitrarily large. When $r \cos \theta > 1$, the Wenzel's Law fails. This corresponds to very high aspect ratio of the rough surfaces. In this case, the surface has to be treated as a composite surface, and one needs to apply Cassie's Law.

1.1.4 Apparent Contact Angle of a Chemically Heterogeneous Surface

When a surface becomes inhomogeneous, one has to consider the effect of different surface energy. The simplest case is a heterogeneous flat surface treated by two different chemicals, with Young's contact angle θ_1 and θ_2 , respectively, as shown in Fig. 1.5. The fractional surface areas occupied by each chemical is f_1 and f_2 , where $f_1 + f_2 = 1$. Similarly, the apparent contact angle θ^* of this heterogeneous solid surface can be obtained by energy

minimization principles as shown in last section. The total free energy change for the contact line displacement dx is (Bico, et al. 1999; Marmur, 2003),

$$dE = f_1 \cdot (\gamma_{1-sl} - \gamma_{1-sv}) \cdot dx + f_2 \cdot (\gamma_{2-sl} - \gamma_{2-sv}) \cdot dx + \gamma_{lv} \cdot dx \cdot \cos \theta^*, \quad (1.6)$$

where γ_{1-sl} and γ_{1-sv} are the surface tensions between solid and liquid, solid and vapor, r for chemical # 1; γ_{2-sl} and γ_{2-sv} are the surface tensions between solid and liquid, solid and vapor, for Chemical # 2. Using the energy minimization principle $dE=0$, one has,

$$\cos \theta^* = f_1 \cos \theta_1 + f_2 \cos \theta_2. \quad (1.7)$$

Equation 1.7 is the well-known Cassie-Baxter's Law, which shows that the apparent contact angle θ^* of a flat heterogeneous surface is the average effect of the two surface components. This law can be, but not limit to, applied to a flat heterogeneous surface with two composites. It is can be extended and generalized to more complicated surfaces with more chemical composites.

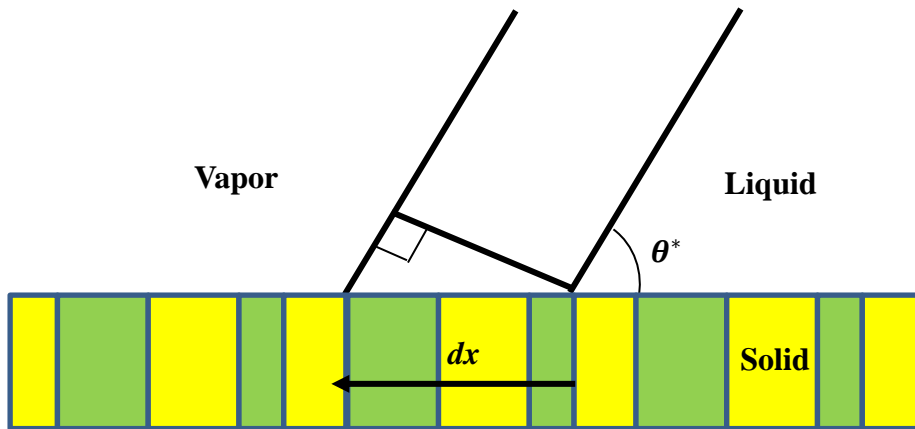


Figure 1.5. The infinitesimal displacement of the three phase contact line on a flat and smooth, but chemically heterogeneous solid surface (move towards the left).

As shown in Fig.1.6, if the flat surface is hydrophobic, the water in the droplet cannot penetrate into the small channels as shown in Fig.1.6 (a). Then effectively the droplet is spreading on a solid-vapor composite surface, and the apparent contact angle θ^* can be expressed as:

$$\cos \theta^* = f_{\text{vapor}} \cdot \cos \theta_{\text{vapor}} + (1 - f_{\text{vapor}}) \cdot \cos \theta, \quad (1.8)$$

where θ is the Young's angle on the flat solid surface, and f_{vapor} is the surface area fraction occupied by water. This situation refers to the Cassie's state.

However, for a hydrophilic surface, the water will penetrate into the channels, as shown in Fig.1.6 (b), effectively the water droplet is spreading on a solid-water composite surface, and the apparent contact angle θ^* can be expressed as:

$$\cos \theta^* = f_{\text{H}_2\text{O}} \cdot \cos \theta_{\text{H}_2\text{O}} + (1 - f_{\text{H}_2\text{O}}) \cdot \cos \theta, \quad (1.9)$$

where θ is the Young's angle on the flat solid surface, and $f_{\text{H}_2\text{O}}$ is the surface area fraction occupied by water. Since $\theta_{\text{H}_2\text{O}} = 0^\circ$, equation (1.8) reduce to

$$\cos \theta^* = f_{\text{H}_2\text{O}} + (1 - f_{\text{H}_2\text{O}}) \cdot \cos \theta. \quad (1.10)$$

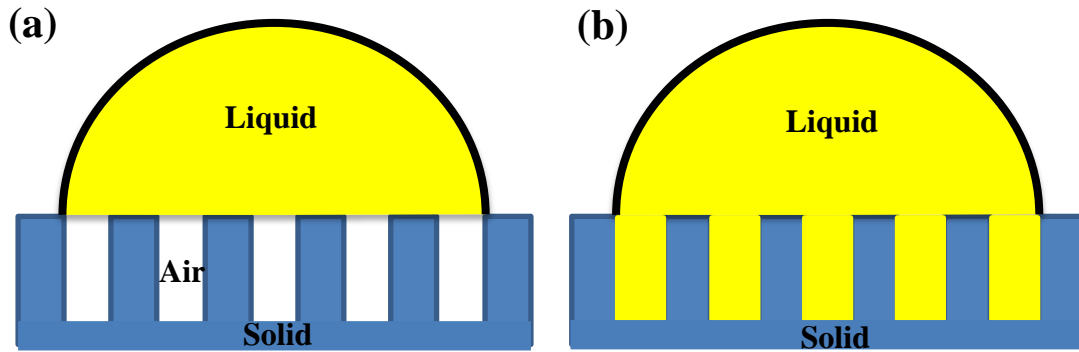


Figure 1.6. A sketch of water resting on a porous solid surface. (a) Water droplet in a Cassie's state. (b) Water droplet in a Wenzel's state.

This situation refers to Wenzel's state. Eq.(1.9) tells us that one cannot induce complete wetting simply by means of introducing the surface roughness, which is different from the prediction by Wenzel's Law.

1.1.5 Sliding Angle

Sliding angle is the maximum angle required for droplet rolling off from a tilted surface. As the surface is inclined, gravity causes the contact angle on the downhill side to increase while the contact angle on the uphill side decreases. Keep increasing the plate titled angle without

moving the three-phase contact line to a maximum. This maximum plate tilted angle is the so-called sliding angle. And the two side contact angles of the sessile drop are referred to advancing and receding angles, respectively.

A real superhydrophobic surface that having the self-cleaning effect, which often requires the static contact angle $\theta^* > 150^\circ$ and low sliding angle θ_s . Fig 1.7 graphically shows the sliding angle measurement with a tilting base method.

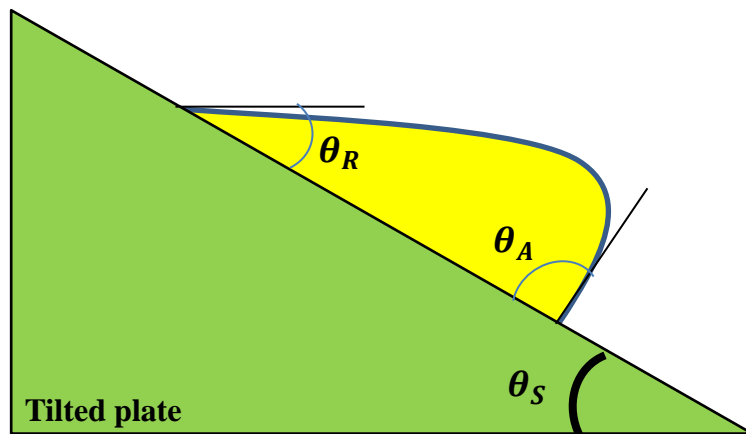


Figure 1. 7. Sliding angle captured by tilting base method.

1.2 Oblique Angle Deposition

Oblique Angle Deposition (OAD) (Young, et al. 1959; Motohiro, et al. 1989; Azzam, et al. 1992; Robbie, et al. 1995; Robbie, et al. 1996; Robbie, et al. 1997; Zhao, et al.2002) is a physical vapor deposition (PVD) at an incident angle (larger than 70°) using a thermal vapor source, which actually is a PVD under conditions of obliquely incident flux and limited adatom diffusion results in a film with a columnar microstructure, has been developed as a technique to engineer the columnar structure of thin films on the micro-and nanoscale. Generally, in OAD, substrate is rotated to an oblique angle relative to the source. The initial vapor nucleation occurred on the

surface can act as seed for subsequent growth of nanorods. And the resulting nanorods are tilted and aligned, but randomly distributed on the surface, as shown in Fig.1.8.

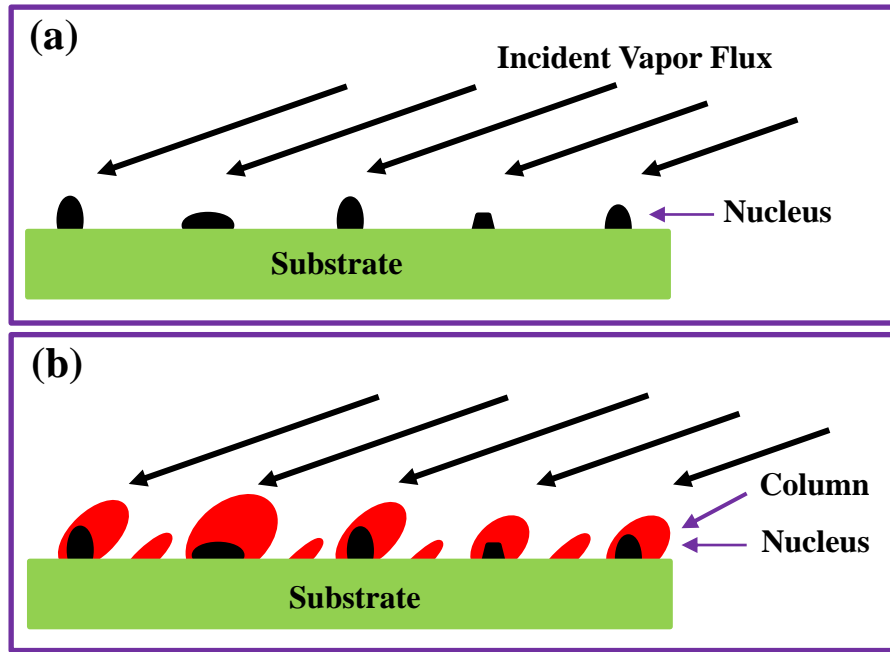


Figure 1.8. Nucleation and shadowing growth. (a) Adatoms condense and nucleation. (b) Column growth as results of shadowing of the initial nuclei and columns will grow oriented towards the direction of incident vapor.

OAD is a highly reproducible, flexible, inexpensive nanofabrication method to generate nanorod arrays relatively easily (Tait et al, 1993; Robbie et al, 1996; Liu et al, 1999; Messier et al, 2000; Zhao et al, 2002). There is almost no restriction on materials since the growth process is a thermal evaporation process, different materials can be fabricated on different substrates, as the samples can be seen in Fig. 1.9.

In addition, OAD also provides controls over nanorod size, shape, orientation, morphology, and density. This unique feature can be used to tune the mechanical, magnetic, and optical properties of the deposited films.

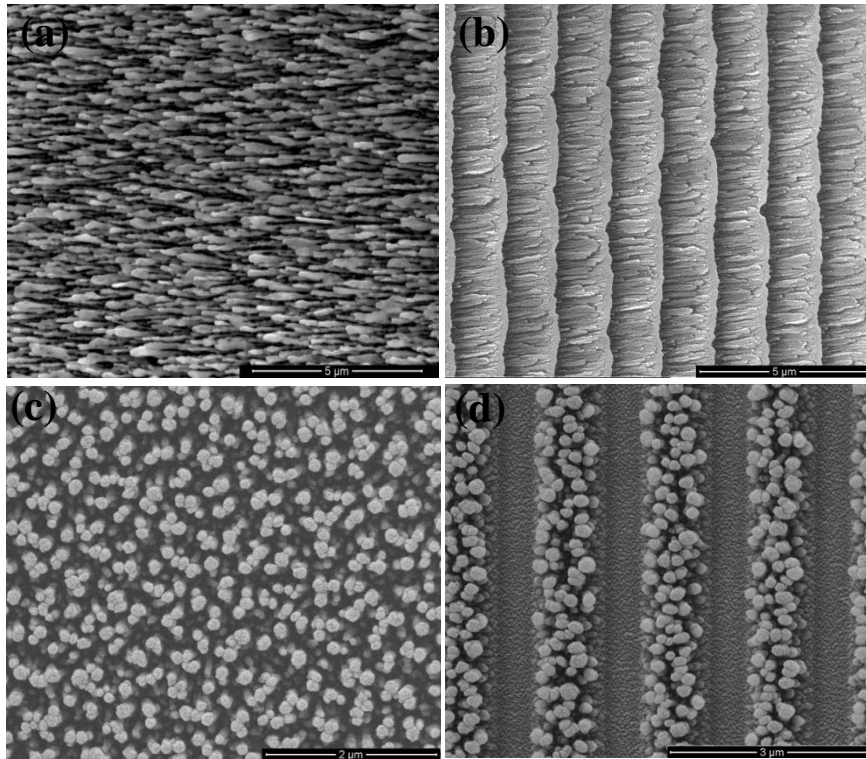


Figure 1.9. SEM images of several nanostructures fabricated by OAD. (a) Ag nanorods array with a length of $\sim 1 \mu\text{m}$ was deposited using the OAD technique at a vapor incident angle of 86° . (b) Si nanorods array with QCM reading 2000nm was deposited by OAD technique on CD surface at a vapor incident angle of 86° . (c) Si nanorods array with QCM reading 2000nm was deposited by OAD technique with substrate rotation at 0.5 rev/s on Si wafer at a vapor incident angle of 86° . (d) Si NR array with QCM reading 2000nm was deposited by GLAD technique with substrate rotation at 0.5 rev/s on CD surface at a vapor incident angle of 86° .

1.3 Current Status of Research in Anisotropic Wetting

The anisotropic wettability has attracted much interest more recently. Anisotropic wettability is achieved either through chemical or topographically patterning. For geometrically or chemically anisotropic structures, alternating and parallel strips with size or chemistry differences, the drop shape will be distorted, and the apparent contact angle is no longer uniform along the contact line, as shown in Fig.1.10.

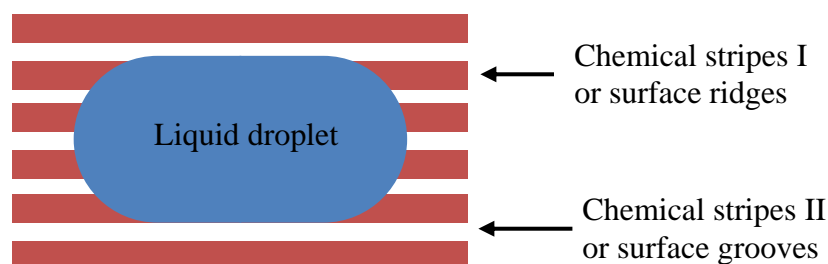


Figure 10. The schematic anisotropic liquid droplet top-view representation.

On one hand, anisotropic wetting control on surface with regular chemical patterns has been studied both theoretically and experimentally. Drelich (1996) reported the anisotropic wetting on the heterogeneous surface consisting of alternating and parallel $2.55\mu\text{m}$ hydrophobic and $2.45\mu\text{m}$ hydrophilic strips. And the advancing and receding contact angles, when measured with the drop edge normal to the strips, were found to be $2\text{-}10^\circ$ lower than those measured with the drop edge parallel to the strips. Gau (1999) presented liquid micro-channels on structured surfaces which are built up using a wettability pattern consisting of hydrophilic stripes on a hydrophobic substrate. The liquid microchannels utilized the anisotropy wetting properties which could be developed into fluid microchips or microreactors. Brandon (2003) also studied the anisotropic wetting of chemically patterned surface theoretically. In the study, the chemically heterogeneous substrates was simulated, and they claimed that contact angle hysteresis observed in this system was shown to exhibit a degree of volume dependence in the advancing and receding angles.

And Morita (2005) also reported the anisotropic wetting on micropatterned organosilane monolayer surfaces with a $1\text{-}20\mu\text{m}$ width, which could be successfully fabricated using a homogeneous fluoroalkylsilane monolayer with few defects by VUV photolithography. In their study, the wetting anisotropy decreased with decreasing in the liquidphilic area of the strips ratios in the range of $1/1$ to $3/1$. And they also claimed that the strong anisotropy of the contact and

sliding angles as well as droplet distortion are due to the difference in the energy barrier of wetting between a line and its orthogonal directions, not the line tension or the asperity.

Bliznyuk (2009) studied the chemically patterned surface which is consisting of alternating hydrophobic and hydrophilic stripes (fluoroalkylsilane SAMs and bare SiO₂ surface, respectively). This chemically heterogeneous surfaces, formed by alternating hydrophilic and hydrophobic stripes with widths in the low micrometer range, gave rise to anisotropic wetting properties. As long as the droplet dimensions are 1–2 orders of magnitude larger than the width of the stripes, these quantities not only depend on the absolute size of the surface pattern, but only depend on the relative width of the hydrophobic and hydrophilic stripes.

Xia (2010) reported another method of using of simple plasma treatments and polymer deposition to tailor the anisotropic wetting properties of onedimensional (1D) submicrometer-scale grooved surfaces, fabricated using interferometric lithography in photoresist polymer films. In this study, low-pressure plasma treatments with different gas compositions (e.g., CHF₃, CF₄, O₂) are employed to tailor the anisotropic wetting properties, without changing the structural anisotropy, from strongly hydrophobic anisotropic to hydrophobic with very high contact angle and superhydrophilic with a smaller degree of wetting anisotropy. It is reported that they can tailor anisotropic wetting while retaining the structural anisotropy using simple and controllable plasma treatments.

On the other hand, anisotropic wetting of topographically patterned surfaces has also been intensively studied both theoretically and experimentally. And some engineered surfaces exhibited anisotropic wetting properties which are derived from asymmetric asperities (Sandre, et al. 1999). For instance, anisotropic surfaces with microscale ratchet-like features have been engineered to transport drops in this manner (Shastry, et al. 2006; Linke, et al. 2006 ; Zhang, et

al, 2009) , although no such surfaces have been synthesized with nanoscale ratchets. However, Malvadkar (2010) reported an engineered thin film, composed of an array of poly (p-xylylene) nanorods, which presented a hydrophobic surface deriving its anisotropic adhesive wetting directly from its asymmetric nanoscale roughness. This hydrophobic surface with anisotropic wetting possesses unique properties, which has inspired tapered tubes and mechanical beaks that propel droplets (Prakash, et al. 2008; Renvois é, et al. 2009). Furthermore, hydrophilic surfaces with anisotropic wetting can control the extent and shape of the wetted area (Courbin, et al. 2007 ; Chu, et al. 2010).

Zhao (2007) reported anisotropic wetting on submicrometer-scale (groove widths of 318, 396, and 513 nm with varying nanometer-scale depth) periodic topographic structures consisting of parallel grooves. The groove depth and wavelength of the structures can be controlled by varying the fluence and incident angle of the laser beam. It was found that the degree of wetting anisotropy and the contact angle hysteresis measured using sessile drops of 3 μ L from the direction perpendicular to the grooves increased with increasing groove depth, which was assigned to the increasing energy barrier to drop spreading caused by pinning of the groove edge, based on a thermodynamic model. However, this submicrometer-scale fabrication did not show a significant wetting anisotropy, which has a degree of anisotropy only 8° and the water droplet distortion aspect ratio nearly 1.

Gao (2007) used a facile laser-etching method for the one-step creation of various controllable dimensions of anisotropic micropatterns consisting of an alternating arrangement of microgrooves and microstripes with rugged nanoprotusions, which after modified with fluoroalkylsilane reagent, showed perfect isotropic superhydrophobicity without apparent CA hysteresis, water adhesion, and drag resistance, other than the conventional view of anisotropic

surface microstructures with anisotropic surface dewetting.

Zhang (2007) fabricated a series of hierarchical structures on polymer films using the technique of sequential imprinting (Zhang and Low, 2006), which is based on conventional nanoimprint lithography (Chou, et al. 1995). These structures allow one to tune the anisotropic wettability on polymeric films without the use of chemical treatment. By using different formats and alignments of patterns in the secondary imprints, various two-level hierarchical structures were formed, which resulted in tunable anisotropic wettability from 6° to 54° .

Similarly, Chung (2007) also reported the anisotropic wetting on tunable micro-wrinkled surfaces, which harnessed a wrinkling instability to produce model substrate topographies. Specifically, they probed the wetting of liquids on anisotropic micro-wrinkled features that exhibit well-defined aspect ratios (amplitude versus wavelength of the wrinkles) that can be actively tuned.

Li (2008) studied the anisotropic wetting behavior arising from superhydrophobic parallel grooved structure surface. They claimed that, for the noncomposite state, decreasing groove width and spacing or increasing groove depth can amplify the anisotropy for equilibrium contact angle. Meanwhile, decreasing groove width and increasing depth can amplify the anisotropy for contact angle hysteresis, while varying groove spacing can barely influence it. For the composite state, however, the surface geometry hardly leads to the anisotropic behavior.

Xia (2009) studied the strongly anisotropic wetting on 1D PR patterned surfaces, the surface wetting was tuned from hydrophobic to hydrophilic using silica nanoparticles while retaining the structural anisotropy. Contact angles, degree of anisotropy, and droplet distortion are measured on micro- and nanopatterned surfaces fabricated with interference lithography. However, in this paper, the mechanism of anisotropic wettability is complex and not

well-understood.

Khare (2009) studied the anisotropic wetting behavior and fluidic transport as a function of surface energy and groove geometry on soft poly (dimethylsiloxane) (PDMS) substrates with 1D sinusoidal wrinkle patterns. And it was found that the contact angle in the direction perpendicular to the grooves is larger than that parallel to the grooves. This wetting anisotropy, for a fixed Young's contact angle, was also found to increase when the grooves become deeper.

Chu (2010) stated that the anisotropic wetting behavior preserves left-right symmetry. They claimed that they can harness the design of asymmetric nanostructured surfaces to achieve uni-directional liquid spreading, where the liquid propagated in a single preferred direction and pins in all others. And they determined that, through experiments and modeling, the spreading characteristic was dependent on the degree of nanostructure asymmetry, the height-to-spacing ratio of the nanostructures, deflection angle and also the intrinsic contact angle.

To summarize, first, most of the current surface modification, both chemically and physically, for anisotropic wetting study mainly focus on a micron or sub-micro scale rather than nanoscale modification, due to technical limitations. There have been few deliberate efforts to demonstrate whether submicrometric, or smaller, features would also lead to the macroscopic distortion of water drops or anisotropic wetting characteristics, and how this would occur, which remains a challenge in this field.

Here, we proposed a Si nanorods aided method to significantly enhance the anisotropic wetting of 1-D Compact Disk grooved surface in a in a nano/ sub-micro meter scale. And also a quantitatively analysis *via* Cassie's Law and Wenzel's Law is proposed to successfully describe the nanostructure's anisotropic wetting behavior as a function of measureable surface morphology parameters.

Furthermore, for the abovementioned research, either chemically or topologically, most of the surfaces with differing wettabilities were produced using various techniques, such as microcontact printing (Kumar, et al. 1994; Xia, et al. 1997; Evans, et al, 1995), micromachining (Abott, et al. 1992), photolithography (Wang, et al. 1997; Calvert, et al. 1993), ultraviolet photolithography (Morita, et al. 2005), interferometric lithography (Xia, et al 2010), optical lithography (Bliznyuk, et al. 2009), which are relatively costly and complex. And also, although lithographic processes are currently the most widely employed and studied techniques for the production of sub-micrometer-sized pattern, however, no dramatic improvements in the accessible sizes should be expected in the future.

1.4 Motivation of This Research

Recently, the control of surface anisotropic wettability has attracted a significant scientific attention in many research areas, including fluid physics, interface physics, biotechnology and materials science. This is mainly driven by sophisticated fabrication technologies, including well-defined chemically and topographically micro/nano-patterned surfaces where wettability is an important design parameter (Kumar et al. 1994; Wouters et al. 2004; Martines et al. 2005). These engineered “smart” surfaces have broad technological applications in industry, including micro- or nanofluidic devices (Grunze 1999; Zhao et al. 2001; Blossey et al. 2003), glass coating and printing (Ma and Hill. 2006; Feng et al. 2004).

Numerous studies in anisotropic wetting have been conducted on topographically anisotropic surface (Chen, et al. 2005; Chung et al. 2007; Zhao et al. 2001) and also chemically heterogeneous surface (Zhao et al. 2001; Zhao et al. 2002; Morita, et al. 2005). More specifically, some researchers mainly resort to physically tuning the duty ratio , aspect ratio or surface roughness of the grooved surface (Sinusoidal or rectangular grooves) to control the surface

anisotropic wettability. And some others presented an experimental study of the tunable anisotropic wetting behavior of the chemically patterned anisotropic surface. Arising from patterns of alternating hydrophilic and hydrophobic stripes with dimensions in the low-micrometer range, water droplet distortion are investigated in relation to stripe widths. However, both surface physical duty ratio tuning and chemical stripes alternating are involving in many sophisticated technologies, such as etching and metallization, which are costly and complex.

Here, we present a fast and simple method, using oblique angle deposition (OAD), to easily generate extended patterned surfaces with controlled wetting properties on the Compact Disk Surface without involving in any complex processing. OAD technique has attracted the interest of many researchers, due to its ability to generate nanostructures relatively easily, conveniently and inexpensively (Tait et al, 1993; Robbie et al, 1996; Messier et al, 2000; Liu et al, 1999; Zhao et al, 2002). Specifically speaking, with oblique angle deposition, one can produce different nano-sized columnar films with controlled porosity and shapes, and also it can form nano-column array naturally. Furthermore, the porosity of the film can be controlled by simply changing the vapor incident angle. In addition, with oblique angle deposition, the shape and in-plane alignment of columns can be easily modified. And also there is almost no restriction on materials for OAD fabrication since the growth process is a thermal evaporation, thus this method should not be restricted to a specific materials and may be extended to other rapidly and easily. Consequently, OAD is an ideal technique which can be well harnessed to fabricate various nanostructures with different anisotropic surface morphology, and thus different anisotropic wetting properties (Wouters and Schubert, 2004).

In addition, the wettability of silicon nanorods depends strongly on the nanorods height

and is easily changeable from hydrophilic to hydrophobic by HFTS treatment (Fan et al, 2003; Fan and Zhao, 2007). This further demonstrated that silicocon nanorods aided method *via* OAD will be an effective and feasible technique to tailor the surface anisotropic wetting properties of compact disk surface with multi-angle.

1.5 Organization of the Thesis

The thesis is arranged in the following manner:

Chapter 2 gives a detailed description of the experimental design and sample preparation procedures. It includes the sample fabrication conditions, SEM characterization, and heptadecafluoro-1,1,2,2-tetrahydrodecyl trichlorosilane (HFTS) treatment for creating superhydrophobic surfaces, and an introduction to sessile droplet method for static contact angle measurement.

Chapter 3 reports the Si nanorods enhanced anisotropic wetting on compact disk surface from hydrophilic perspective. We compared the wetting properties of Si wafer, CD, CD coated with Si and SiNR coated CD samples, and found that the SiNR deposited perpendicularly to the CD grooves can greatly enhance the anisotropic wetting of the surface.

Chapter 4 studies the Si nanorods enhanced anisotropic wetting on compact disk surface from hydrophobic perspectives. By modifying the silicon surface with HFTS, the surface will become hydrophobic. How would the hydrophobicity change as the surface morphology change is a very interesting problem, and we focus on answering this question in this chapter.

Chapter 5 summaries all the results and gives some future prospects.

CHAPTER 2

EXPERIMENTAL DESIGN AND PREPARATION

This Chapter gives a detailed description of the experimental design and preparation: sample characterization and measurement conditions. Specifically, it is about the sample fabrication, SEM characterization, and HFPS treatment for creating hydrophobic surfaces. Furthermore, a systematic introduction of Sessile Droplet Method for static contact angle measurement will be presented. In addition, a brief introduction to the sliding angle measurement as well as watermark photography will be particularly rendered.

2.1 Substrate Preparation

Silicon Wafer: The silicon wafer (Montco Silicon Technologies, Inc. P/Boron<100>, 100+/-0.5mm) was cut into 3cm × 2 cm size. And they were cleaned by the mixture of DI water : Hydrogen peroxide: Ammonium hydroxide with a volume ratio of 5:1:1 for 30 min followed by DI water rinsing and compressed nitrogen (N₂) blow drying, and were served as the substrates for deposition.

CD Substrate: The CD (MAM-A / Mitsui. Inc. MAM-A color thermal) was etched in nitric acid (68%-70%, EMD Chemicals. NX0409-75) for 30 seconds, rinsed in the DI water flow for about 2 minutes, and dried in compressed nitrogen for about 2 minutes. Then the CD was cut into 1.5cm × 1.5cm pieces by a scissors, as shown in Fig.2.1. The edges of the CD pieces were smoothed by a single edge razor blade (Garvey Products. Inc.). After removing the flakes by compressed nitrogen the CD pieces were rinsed again in the flowing DI water. Finally, the CD

substrates will be dried by the compressed nitrogen and loaded onto the sample holder for deposition.

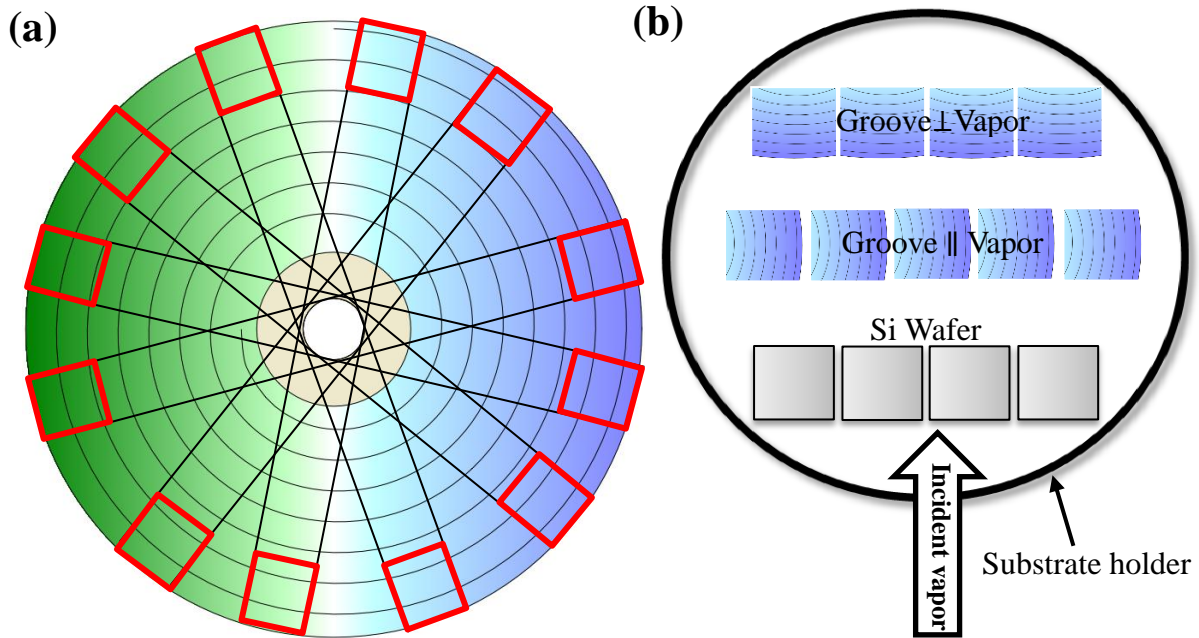


Figure 2.1. Substrates arrangement for oblique angle deposition. (a) A sketch shown cutting the CD. (b) The substrate arrangement on a substrate holder.

Since the CD has grooves, the substrates were loaded to the substrate holder according to Fig. 2.1. The bottom row was silicon wafers, the middle row were CD samples with grooves parallel to the vapor incident direction, and the top row was CD samples with grooves perpendicular to the vapor incident direction.

2.2 Sample Fabrication

All the samples, both silicon thin film and Silicon nanorods (SiNR), were fabricated using a custom-designed electron beam-sputtering evaporation system (Torr International Inc., NY), as figure 2.2 shows. The substrates were positioned in the vacuum chamber so that the vapor incident direction was at a certain angle with respect to the surface normal of the substrates for thin film or nanorods deposition. During the evaporation, a Quartz Crystal Microbalance (QCM) directly facing the vapor was used to monitor both the thickness and the rate of the deposition.

The basic principles of oblique angle deposition were previously detailed introduced in the thesis section 1.2.

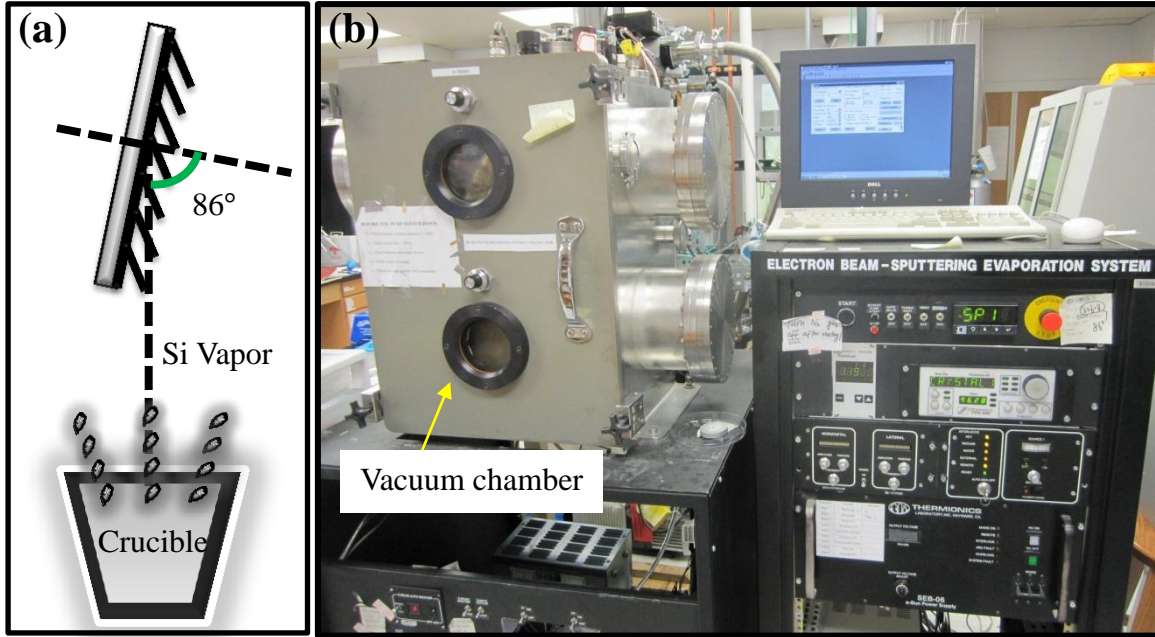


Figure 2.2. Custom-designed electron beam-sputtering evaporation system for OAD. (a) A sketch of the setup for template oblique angle deposition. (b) Photograph of electron beam-sputtering evaporation system in our lab for OAD.

As regarding of the nanorod deposition, first, a very thin layer of Ti was deposited onto the substrates as an adhesion enhancing layer. In order to ensure a full coverage of Ti, we designed the following procedure: first deposit a layer of 10nm Ti with vapor incident angle $\alpha = 0^\circ$, then the substrates were rotated to $\alpha = 45^\circ$, we deposited another 10nm Ti, and finally the substrates were rotated to $\alpha = -45^\circ$ with 10 nm Ti deposition.

After Ti deposition, we deposited the silicon thin film followed the same strategy of Ti deposition. In this case, each Si deposition was 20 nm thick. Finally, Si nanorod arrays were deposited at $\alpha = 86^\circ$ follow Fig. 2.1(b). For SiNR fabrication, the Si deposition rate was set at 0.2nm/s with a QCM thickness of 2000 nm and the chamber pressure keeps below 3×10^{-6} Torr.

2.3 SEM and AFM Characterization

The morphologies of all the samples were characterized by a field-emission scanning electron microscope (FE-SEM) (FEI, Inspect F). The morphology of the polymer-stripped-off CD surface was characterized by the atomic force microscopy (AFM, Veeco Metrology Group).

2.4 Chemical Treatment

After Si deposition, the surface will be hydrophilic due to the formation of nature oxide layer. To make the surface hydrophobic, we perform a chemical treatment for the as-deposited samples. Specifically, a self-assembled HFTS monolayer was created (Heptadecafluoro-1,1,2,2-tetrahydrodecyl) trichlorosilane (Gelest, Inc. CAS 78560-44-8) on silicon thin film or nanorods surface by mean of chemical vapor surface modification (CVSM) method. This layer of HFTS SAM could tailor the surface wetting properties from hydrophilic to hydrophobic.

The HFTS is a silane ($C_{10}H_4C_{13}F_{17}Si$) with molecular structure, as shown in Fig. 2.3. The molecule length of the HFTS is about 1.7 nm (Tada and Nagaysma, 1994) and the critical surface tension of the $-CF_3$ group is about 6 mN/m, which is the lowest critical surface energy ever reported (Shibuichi, et al. 1998) and can be perfectly used to tailor the surface wetting property into hydrophobic .

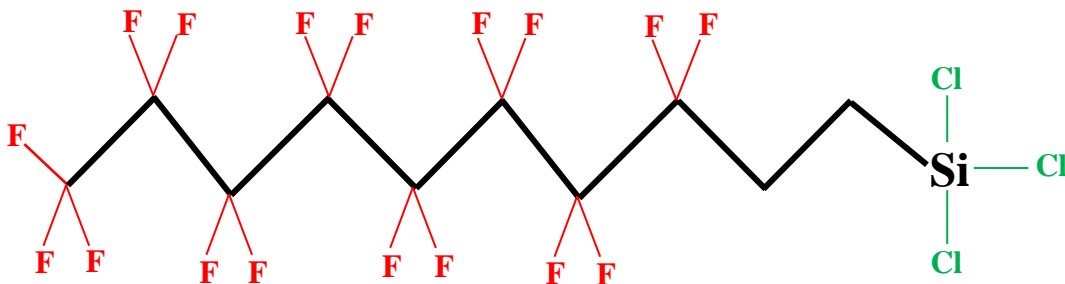


Figure 2.3. Molecular structure of HFTS

To form HFTS SAM on Si surfaces, we used a chemical vapor surface modification (CVSM) method. The experimental setup is shown in Fig. 2.6. The as-deposited samples were loaded onto the aluminum latticed interlayer in the middle of a Wheaton Vacuum Chamber (Fisher Scientific) as shown in Fig. 2.4.

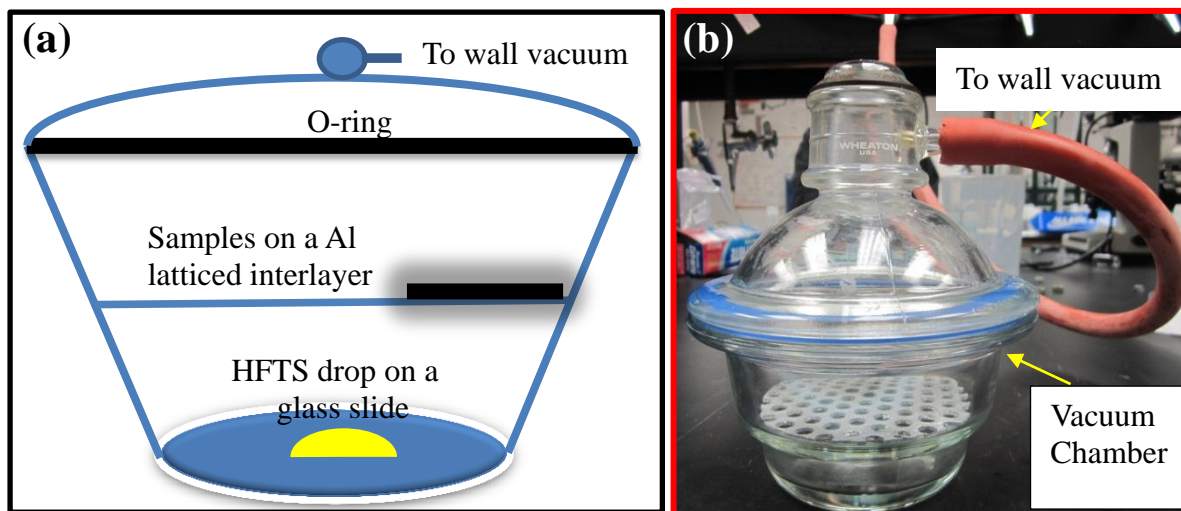


Figure 2.4. (a) The CVSM setup for HFTS SAM creation. (b) Photograph of the CVSM setup in our lab.

A droplet of 60 μ l HFTS was pipetted in bottom of the vacuum chamber. Then, the chamber was pumped down using the wall vacuum. After about 22 hours, the samples were taken out from the chamber, rinsed with DI water, and dried with compressed N₂.

The contact angle measured on the HFTS modified Si wafer by CVSM technique with a sessile drop method is $113 \pm 1^\circ$, as shown in figure 2.5 (b), which is consistent with the contact angle value reported by Tada (Tada and Nagayama, 1994). And also, similarly, we used CVSM technique to create a layer of HFTS SAM onto the glass wafer, which gave us a static contact angle of $113.5 \pm 0.5^\circ$, as can be seen in the figure 2.5(d).

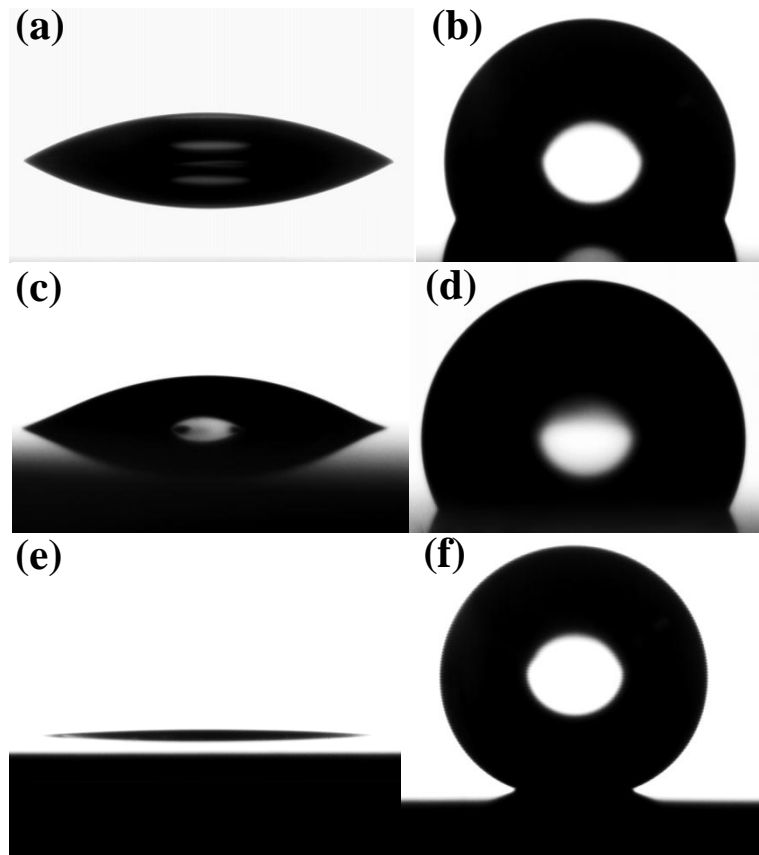


Figure 2.5. Static contact angle (CA) measurement on the samples before or after HFTS treatment. (a-b) Static contact angle measurement on silicon wafer. Before HFTS treatment: CA=28.5°. After HFTS treatment, CA=113.9°. (c-d) Static contact angle measurement on glass wafer. Before HFTS treatment: CA=27.2°. After HFTS treatment, CA=113.5°. (e-f) Static contact angle measurement on QCM reading 1000nm Si nanorods, fabricated with GLAD technique with rotation speed 0.005 rev/s at 86° vapor incident angle. Before HFTS treatment: CA=3.2°. After HFTS treatment, CA=155.6°.

2.5 Sessile Droplet Method

The contact angles of the Si wafer, coated CD surfaces and HFTS treated substrates were measured by a sessile droplet method. The sessile droplet method measures the droplet contour on the surface through an optical system as shown in Fig.2.6.

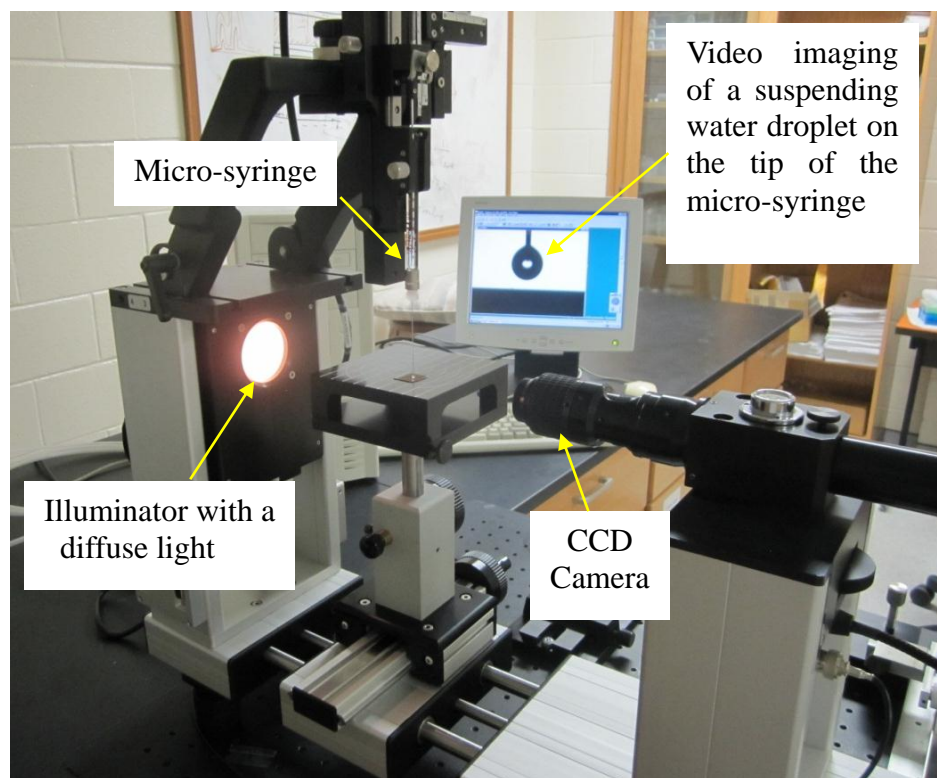


Figure 2.6. The contact angle measurement system (Data Physics OCA 20) in our lab: a liquid droplet (DI water for all my experiments) is deposited onto the samples' surface through a microsyringe, the contour the liquid droplet is captured by a CCD camera.

We used the SCA 20 (Software for OCA and PCA) to perform the contact angle measurements. After capturing the droplet shape, the contact angle was determined by fitting the droplet contour. Here we used Young-Laplace fitting with a fixed droplet volume of $2\mu\text{l}$.

2.6 Sliding angle Measurement

The sliding angle of a water droplet on the hydrophobic surface were measured by a home-made setup shown in Fig.2.7. A water droplet with fixed volume of $10\mu\text{l}$ was dispensed onto the sample surface by a microsyringe. Then the substrate was tilted slowly until we reach a critical angle θ_s , where the droplet started to trolling down along the slope. This angle can be simply read by a vernier attached to the setup.

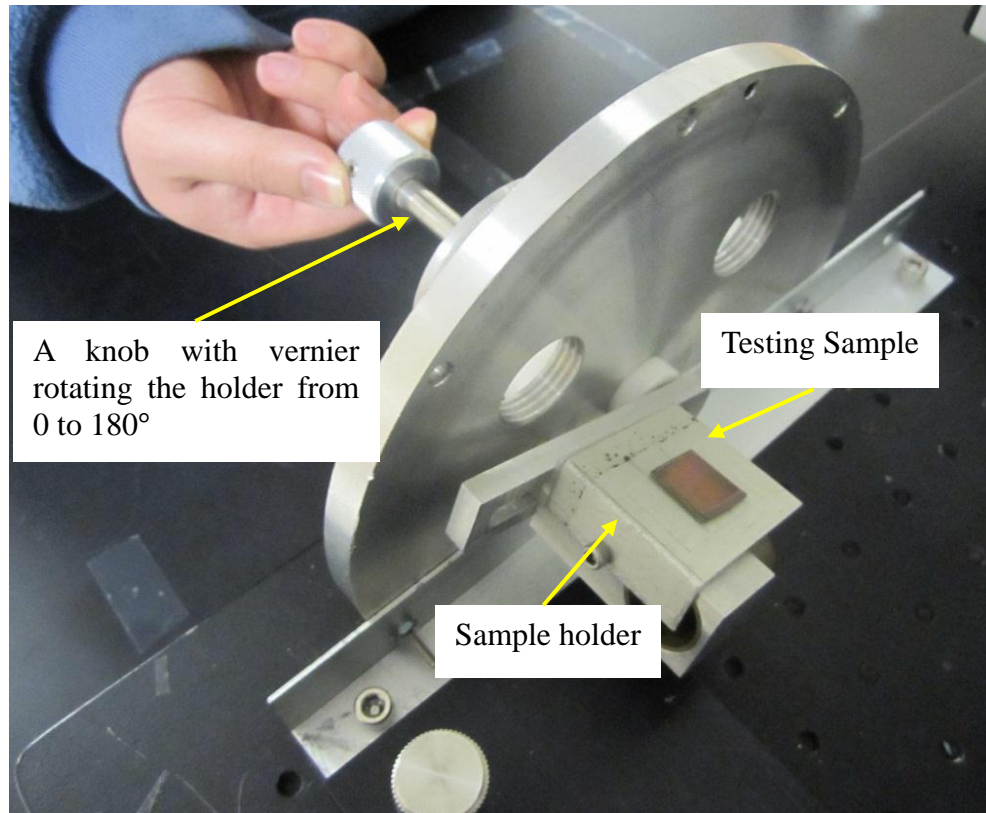


Figure 2.7. A custom built system for sliding angle measurement.

2.7 Watermark and Droplet Shape Photography

The droplet shape after a 2- μ l water droplet was dispensed onto the surface were recorded by Digital Camera (Cannon SD940) with the shape size larger than 1 mm.

When the shape size is smaller than 1mm, obtaining a clear view of the droplet shape is beyond the capacity of a common digital camera, and thus, a Phantom digital high speed image system is used, as can be seen in Fig.2.8.

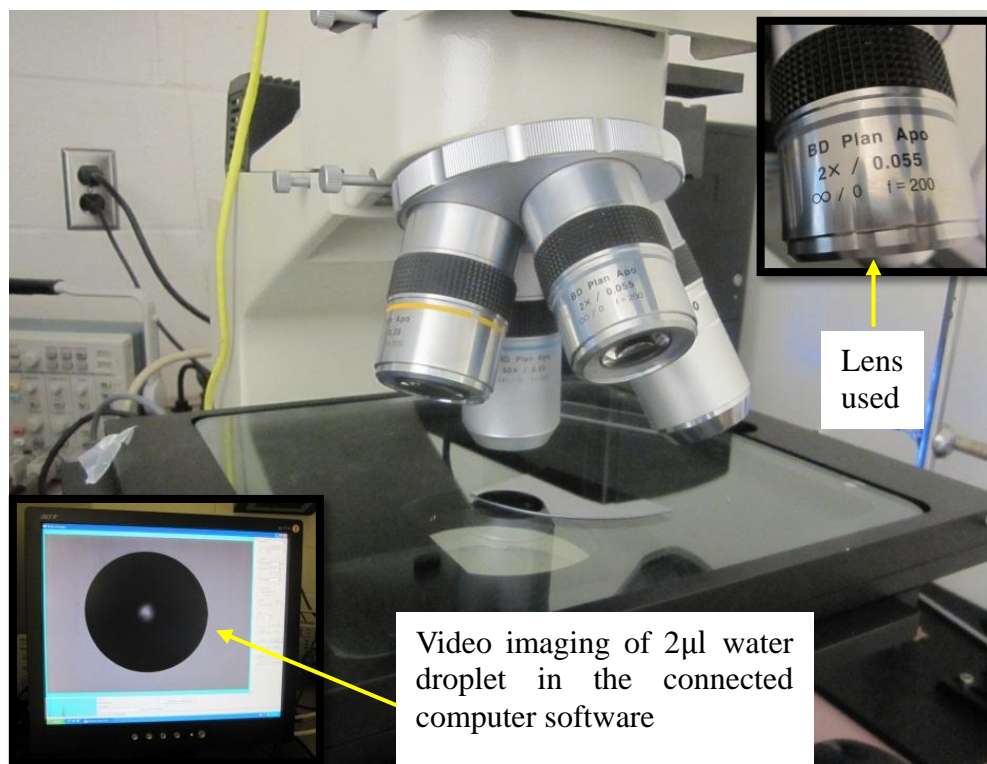


Figure 2.8. Phantom digital high speed image system for photography of the water droplet resting on the samples in a millimeter scale.

CHAPTER 3

HYDROPHILIC ANISOTROPIC WETTING

In this chapter, we report our experimental results on the hydrophilic surface. We compared the wetting properties of Si wafer, CD, CD coated with Si and SiNR coated CD samples, and found that the SiNR deposited perpendicularly to the CD grooves can greatly enhance the anisotropic wetting of the surface, while the SiNR grooves parallel to the CD grooves did not show significant anisotropy. And the experimental results indicate that the SiNR \perp CD sample demonstrates a significantly enhanced anisotropic wetting behavior, tailoring the surface wetting anisotropy by increasing the watermark aspect ratio from 1.17 to 4.57. The contact angle of the SiNR \perp CD sample also showed anisotropy: the contact angle parallel to CD groove $\theta_{\perp} = 16 \pm 2^{\circ}$, and the contact angle perpendicular to the surface groove $\theta_{\parallel} = 6.8 \pm 0.5^{\circ}$. We have used both Cassie's Law and Wenzel's Law to interpret the contact angle changes quantitatively for different substrates.

3.1 EXPERIMENTAL RESULTS

3.1.1 The wetting of CD or Si film modified CD

The wetting properties of CD and Si film modified CD were characterized as the references. Fig.3.1 shows the corresponding droplet shape and contact angle when a 2- μ l water droplet was placed on a stripped CD surface. We can see that from top view, the droplet elongated along the CD groove direction. We define the direction along the CD groove as $x(\parallel)$

direction, and the direction perpendicular to CD groove as $y(\perp)$ direction as shown in Fig. 3.1 (a). Then the droplet shape aspect ratio η is defined ratio of the elongated direction diameter L to the $y(\perp)$ direction W , as can be seen in Fig.3.1. For this particular case, we have $L=3.50 \pm 0.01\text{mm}$ and $W=2.95 \pm 0.01\text{mm}$, so $\eta = 1.19$. And the static contact angle viewing in the $y(\perp)$ and $x(\parallel)$ direction are also different with a $\theta_{\perp}=25\pm 3^{\circ}$ and $\theta_{\parallel}= 21\pm 1^{\circ}$

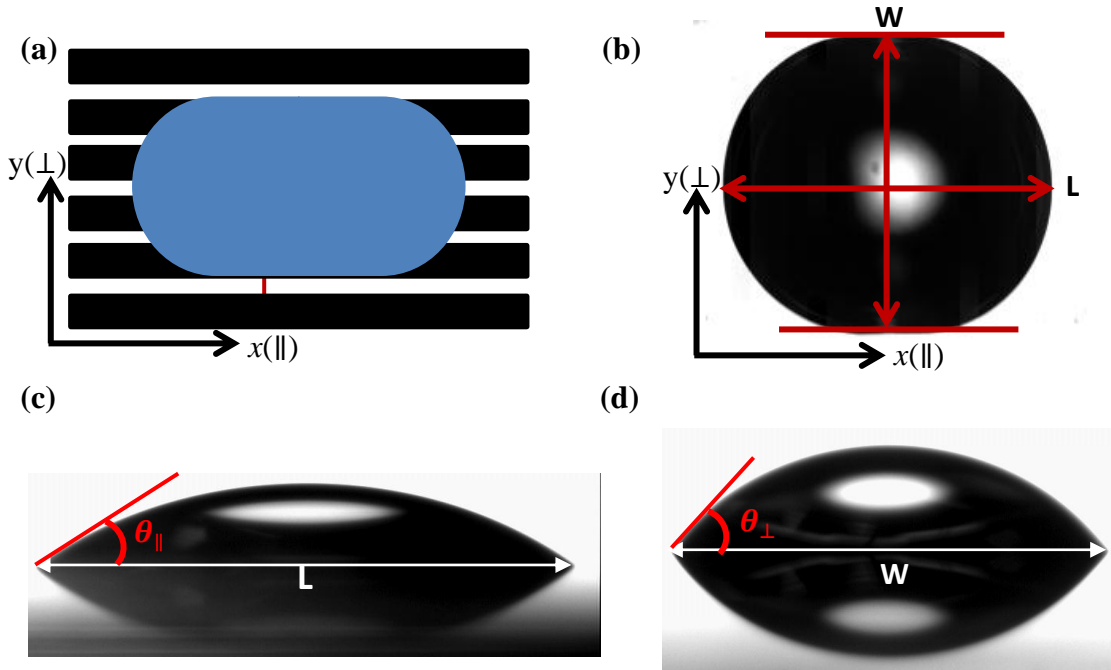


Figure 3.1. Anisotropic droplet quantitative analysis: (a) schematic water droplet top-view representation and (b) photograph of an asymmetric DI water droplet on a polymer-stripped-off CD surface with an aspect ratio 1.17, which is defined by the ratio of its length to width, where length L is the size of the watermark along the surface grooves and the width W is the size of the watermark perpendicular to the surface grooves. (c-d) The water droplet profile and static contact angle measurement demonstration.

Table 3.1. Static Contact Angle Measurement on Si Thin Film Modified Surface

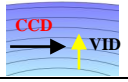
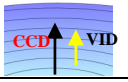
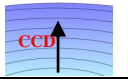
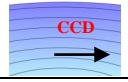
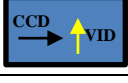

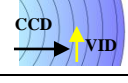
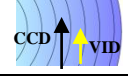
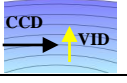
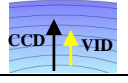
Chemical Treatment	Silicon Wafer		CD Substrate			
	Si Wafer as a control	Si thin film Modified	Si Modified	Si Modified	Bared CD	Bared CD
Without HFTS	$28.5 \pm 0.5^\circ$	$28 \pm 1^\circ$				
HFTS Treated	$114 \pm 1^\circ$	$118.3 \pm 0.3^\circ$	$128.5 \pm 0.6^\circ$	$124.8 \pm 0.5^\circ$	–	–

Table 3.2. Static Contact Angle Measurement on SiNR Modified Surface


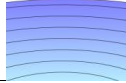
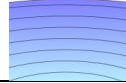
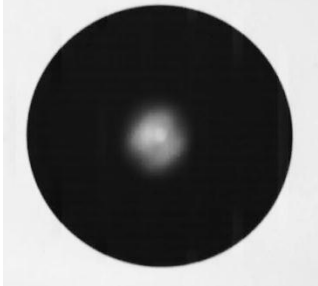
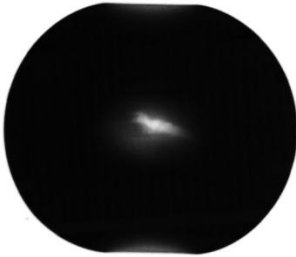
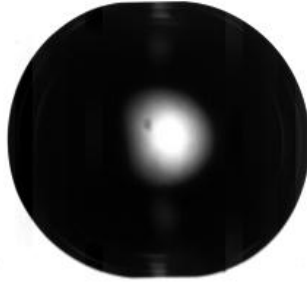
After Si thin film modification, QCM reading 2000nm SiNR will be grown onto CD or Si wafer *via* OAD at 86° vapor incident angle

Chemical Treatment	Si Wafer		CD Substrate			
	SiNR modified	SiNR modified	SiNR modified	SiNR Modified	SiNR Modified	SiNR Modified
Without HFTS						
HFTS Treated	$141.5 \pm 0.3^\circ$	$139.6 \pm 0.5^\circ$	$141.7 \pm 0.9^\circ$	$142.2 \pm 0.4^\circ$	$145 \pm 1^\circ$	$140.7 \pm 0.3^\circ$

Annotation for table 3.3 and 3.4:

1. CCD : The center line of CCD (Data Physics OCA 20) when we measure the static contact angle by the sessile drop method with a fixed 2 μ L water droplet.
2. VID : The Vapor Incident Direction when we fabricated nanorod by the OAD method using a custom-designed electron-beam evaporation system.
3. TD: The sample tilted direction when we measure the sliding angle with a fixed 10 μ L water droplet.
4. For all the samples, we firstly deposit 10nm Ti thin film onto the substrates (CD and silicon wafer) respectively with 0°/45°/-45° vapor incident angle, as an adhesion enhancing layer.

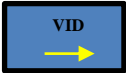

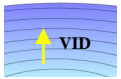
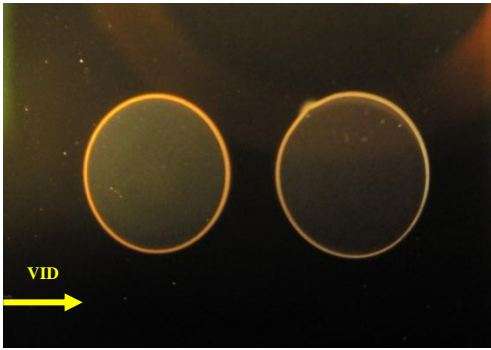
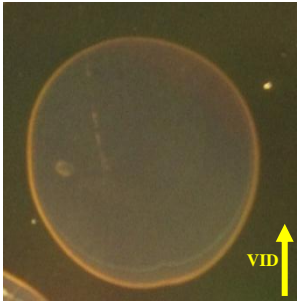
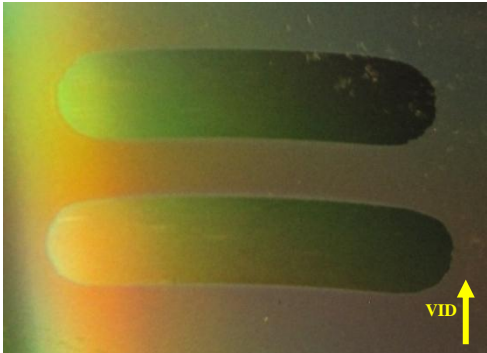
Table 3.3. Water Droplet on Si Thin Film Modified Samples

Without HFTS Treatment	Silicon Wafer	CD Substrate	
	Si thin film Modified Si wafer	Si thin film modified Bared CD	Bared CD
			
Water droplet Top-view			
Size (mm)	Diameter: 3.16 ± 0.03	L: 3.50 ± 0.01 W: 2.95 ± 0.01	L: 2.43 ± 0.01 W: 2.08 ± 0.01
Aspect Ratio $\eta = L/W$	1	1.19	1.17

Annotation for table 3.1 and 3.2:

1. Degree of Anisotropy characterizes the distortion of three phase contact line in the anisotropic wetting. In the thesis, we use the aspect ratio or the watermark or water droplet to represent and evaluate the degree of anisotropy.
2. For the watermark or droplet distortion characterization part, the volume of all the used water droplet is fixed at $2\mu\text{l}$.

Table 3.4. Watermark on SiNR Modified Samples

After Si thin film coating, QCM reading 2000nm SiNR will be grown on CD or Si wafer <i>via</i> OAD at 86° vapor incident angle							
	Si Wafer		CD Substrate				
Chemical Treatment	SiNR modified Si Wafer		SiNR modified With Parallel Growth		SiNR Modified with Vertical Growth		
							
Without HFTS Watermark							
Size (mm)	L: 4.94 ± 0.04	W: 4.51 ± 0.03	L: 5.26 ± 0.04	W: 4.89 ± 0.05	L: 11.98 ± 0.05	W: 2.62 ± 0.06	
Aspect ratio $\eta = L/W$	1.10		1.08		4.57		

3.2 DATA INTERPRETATION AND DISCUSSION

In this experimental results discussion section, a theoretical interpretation to all the static contact angles and also the watermark aspect ratio on the hydrophilic surface will be particularly provided.

3.2.1 Static Wetting Study and Comparison

3.2.1.1. Silicon thin film modified Silicon wafer vs. SiNR modified Si wafer

According to table 3.1 and 3.2, we can get to know the contact angle of these two samples as following:

Silicon thin film modified Silicon wafer: $\theta_{Si} = 28 \pm 1^\circ$

Si nanorod modified Silicon wafer: $\theta_{SiNR-\parallel} = 10.8 \pm 0.6^\circ$ (CCD \perp VID)

$\theta_{SiNR-\perp} = 9.7 \pm 0.9^\circ$ (CCD \parallel VID)

Basically, we can consider the surface of Si nanorod modified silicon wafer as a rough, but chemically homogeneous surface. And it can be considered as a kind of porous material, in/on which the liquid can be absorbed (Bico, et al. 2001). We can image that some liquid escapes from the droplet and penetrates into the nooks and crannies of the solid. The droplet could find itself essentially on a wet surface viewed as patches of silicon and water, this is also the so-called *hemi-wicking*.

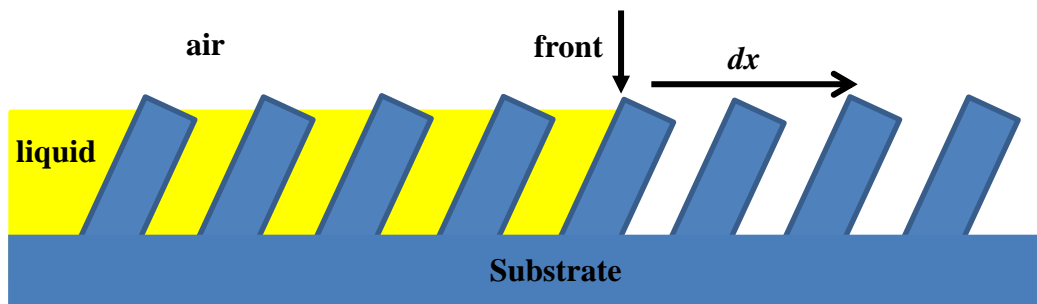


Figure 3.2. A sketch for the *Hemi-wicking*. The water film propagates from a deposited drop, a small amount of liquid is sucked into the tilted silicon nanorods, and then spread across the water-silicon composite to form the equilibrium contact angle.

Reasonably, we can assume that when a film propagates from a deposited drop, a small amount of liquid is sucked into the tilted silicon nanorods, and the remaining drop sets on a patchwork of solid and liquid. According to Cassie's Law, the apparent contact angle θ_{SiNR} can be expressed as:

$$\cos \theta_{\text{SiNR}} = \phi_S \cdot \cos \theta_{\text{Si}} + 1 - \phi_S. \quad (3.1)$$

where ϕ_S is the silicon nanorods fraction remaining dry, for larger height $h > 150$ nm, it is constant at about 0.2 (Fan, et al. 2004). Given $\theta_{\text{Si}} = 28 \pm 1^\circ$, equation 3.1 yields a θ_{SiNR} of $11.1 \pm 0.9^\circ$, which is very close to our experimental results.

3.2.1.2 Silicon thin film modified Silicon wafer vs. Silicon thin film modified CD substrate

According to table 3.1, we can get to know the contact angle of these two samples as following:

Si nanorod modified CD substrate: $\theta_{\text{Si-CD-}\perp} = 21 \pm 1^\circ$ (CCD \perp Groove)

$\theta_{\text{Si-CD-}\parallel} = 25 \pm 3^\circ$ (CCD \parallel Groove)

Likewise, we can take the surface of Si thin film modified CD substrate as a rough, but chemically homogeneous surface. And the surface roughness is introduced by the CD surface grooves. Specifically, we assume that the surface roughness is $r_{\text{Si-CD-}\parallel}$ and $r_{\text{Si-CD-}\perp}$, respectively corresponding to the apparent contact angle $\theta_{\text{Si-CD-}\parallel}$ and $\theta_{\text{Si-CD-}\perp}$.

According to Wenzel's Law, we can obtain following equations,

$$\cos \theta_{\text{Si-CD-}\parallel} = r_{\text{Si-CD-}\parallel} \cdot \cos \theta_{\text{Si}}, \quad (3.2)$$

and

$$\cos \theta_{\text{Si-CD-}\perp} = r_{\text{Si-CD-}\perp} \cdot \cos \theta_{\text{Si}}. \quad (3.3)$$

Submit the experimental results of contact value of $\theta_{\text{Si-CD-}\parallel}$, $\theta_{\text{Si-CD-}\perp}$ and θ_{Si} into Eq. (3.2) and Eq.(3.3), respectively, by calculation, we can obtain the surface roughness $r_{\text{Si-CD-}\parallel} = 1.03$ and $r_{\text{Si-CD-}\perp} = 1.06$. This can be confirmed by AFM measurement of CD.

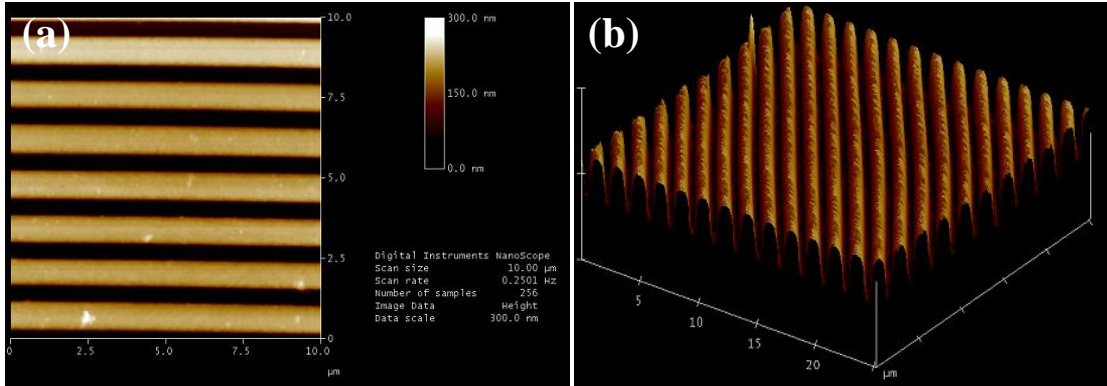


Figure 3.3. An AFM characterization of the polymer-stripped-off CD surface. (a) Top view of $10 \times 10 \mu\text{m}^2$ topographic image and (b) 3D view of the $25 \times 25 \mu\text{m}^2$ topographic image.

An AFM characterization of the CD surface is given out in Figure 3.3. The AFM pictures analysis is carried out with the Nanoscope Control Software (Quadrex, Digital Instrument) and the bared CD has an average periodicity $1.429 \pm 0.006 \mu\text{m}$ and a depth $178 \pm 5 \text{nm}$. Thus, we assume the profile mathematical function is,

$$y = f(x) = A \cos \omega x \quad , \quad (3.4)$$

where $A = 89 \text{ nm}$, $\omega = 2\pi/\lambda$ and $\lambda = 1429 \text{ nm}$.

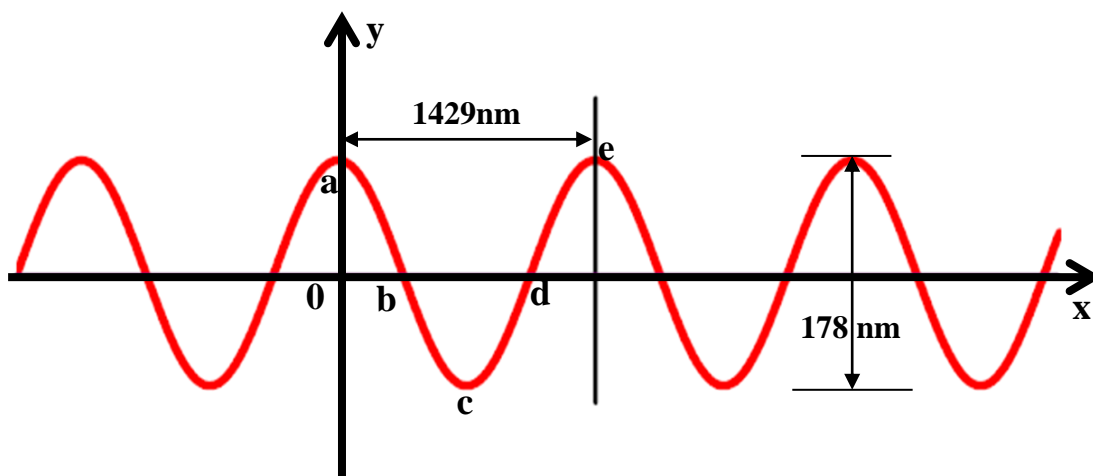


Figure 3.4. A mathematic description of the CD surface profile, based on the measured surface parameters by Atomic force microscopy (AFM, Veeco Metrology Group)

We can estimate the surface roughness $r_{\text{Si-CD}}$ induced by the grooves as following:

$$r_{\text{Si-CD}} = S_{\text{abcde}} / \lambda, \quad (3.5)$$

and
$$S_{\text{abcde}} = 4 \int_0^{\frac{\lambda}{4}} \sqrt{(1 + (-A\omega \sin \omega x)^2)} \cdot dx, \quad (3.6)$$

where S_{abcde} is arc length along the cosinodal function. *Via* MATLAB programming, we can obtain $S_{\text{abcde}} = 1482$ nm, which results a predicted $r_{\text{Si-CD}} = 1.04$. This is well consistent with the roughness factor obtained from Wenzel's law. Detailed calculation could be found in Appendix A.

3.2.1.3 Silicon thin film modified Silicon wafer vs. SiNR vertical growth on CD substrate

According to the experimental data from table 3.3 and table 3.4, we can get to know the contact angle of SiNR vertical growth on CD substrate as following:

$$\text{SiNR vertical growth on CD substrate: } \theta_{\text{SiNR-CD-V}_{\parallel}} = 16 \pm 2^{\circ} \text{ (CCD} \parallel \text{Groove)}$$

$$\theta_{\text{SiNR-CD-V}_{\perp}} = 6.8 \pm 0.5^{\circ} \text{ (CCD} \perp \text{Groove)}$$

The SiNR modified CD surface can be view as a very rough hydrophilic surface. We can apply the classic Cassie's law,

$$\cos \theta_{\text{SiNR-CD}} = f_{\text{H}_2\text{O}} + (1 - f_{\text{H}_2\text{O}}) \cos \theta_{\text{Si}}, \quad (3.7)$$

where $\theta_{\text{Si}} = 28 \pm 1^{\circ}$, and $f_{\text{H}_2\text{O}}$ is the surface area fraction occupied by water after the droplet spreading on the surface of the nanorod structure. From the measured contact angle, one can obtain that $f_{\text{H}_2\text{O}} = 0.66 \pm 0.08$.

The SEM images of the surface are shown in Fig. 3.5, based on the surface morphology, we can estimate $f_{\text{H}_2\text{O}}$ theoretically.

After we deposited a water droplet onto the sample, after wetting, the silicon nanorods could be bundled together due to nanocarpet effect (Fan, et al. 2004; Fan and Zhao, 2006).

Consequently, we can treat the surface as bundled silicon nanorod as shown in Fig. 3.6. And finally, the droplet will find itself essentially resting on a wet surface viewed as patches of silicon and water.

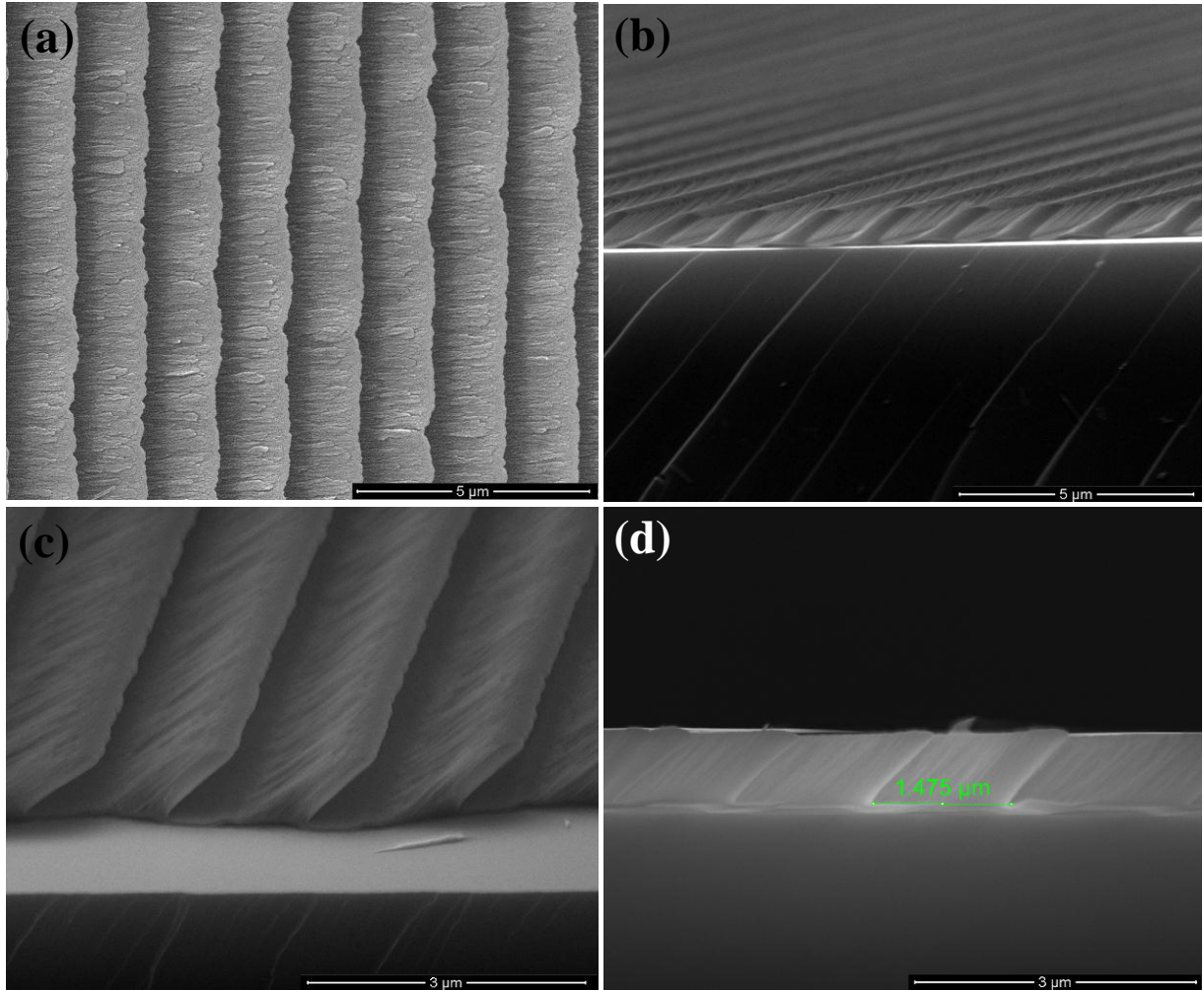


Figure 3.5. SEM image of SiNR on the CD surface with vertical growth. (a) Top view. (b-c) Oblique view. (d) Cross section view.

The water film invades the texture of the solid decorated with sub-microchannels. Due to nanocarpenter effect, the bundling tilted silicon nanorods forms parallel aligned silicon walls. If we deposit a water droplet onto the sample, the water will spontaneously fill the grooves very quickly, and resting in the *hemi-wicking* state, the surface area fraction occupied by water could be estimated by the following equation:

$$f_{\text{H}_2\text{O}} = (1429\text{nm} - 423\text{nm})/1429\text{nm} = 0.704. \quad (3.8)$$

This result is consistent with the experimental result from equation 3.6, that the surface area fraction occupied by water should be 0.66 ± 0.08 .

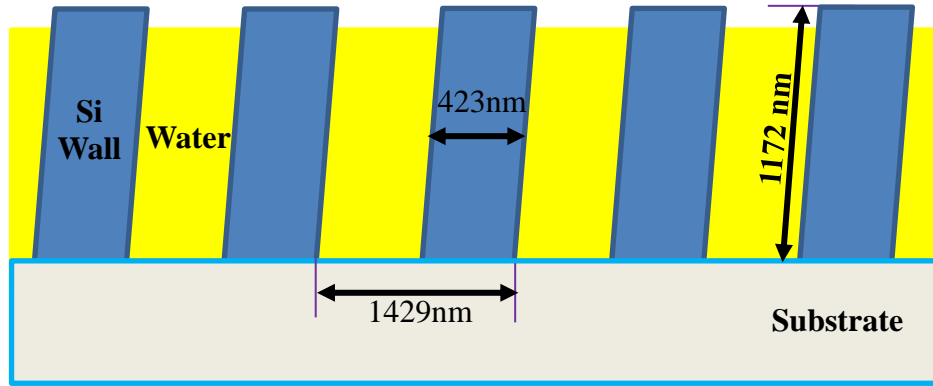


Figure 3.6. The model of the surface profile of SiNR on CD substrate with vertical growth.

However, as regarding of the contact angle $\theta_{\text{SiNR-CD-V}_\perp} = 6.8 \pm 0.5^\circ$, for which the center line of the CCD is vertical to the CD grooves, we are capable of giving a well explanation based on a free energy thermodynamic analysis (Li, et al. 2005; Li, et al. 2008; Long, et al. 2006).

Specifically, in the thermodynamic methodology, the free energy (FE) curves clearly shows different configurations of free energy barrier (FEB), such as shape, size, and frequency of occurrence, for different directions towards the surface grooves (Li, et al. 2008). Usually, there are a great number of FEBs in the direction of perpendicular to the surface grooves. This may therefore cause the pin effect of the three-phase contact line because of numerous metastable states, when a droplet advances on the grooved surface around this direction. As a result, the apparent CA perpendicular to the surface grooves are very close to the advancing CA, in our experimental result, which is $\theta_{\text{SiNR-CD-V}_\parallel} = 16 \pm 2^\circ$.

However, in direction of parallel to the surface grooves, wetting metastable states with lower FE will easily be attained due to the less number of FEBs, which is thus expected to be

smaller than contact angle in the groove perpendicular direction, in our case, which is $\theta_{\text{SiNR-CD-V}_\perp} = 6.8 \pm 0.5^\circ$. Detailed discussion could be found in appendix B.

3.2.1.4 Silicon thin film modified Silicon wafer vs. SiNR parallel growth on CD substrate

The static contact angle of SiNR on CD substrate with parallel growth are:

$$\theta_{\text{SiNR-CD-P}_\parallel} = 14 \pm 3^\circ \text{ (CCD } \parallel \text{ Groove)}$$

$$\theta_{\text{SiNR-CD-P}_\perp} = 13 \pm 2^\circ \text{ (CCD } \perp \text{ Groove)}$$

Similar to discussion in section 3.2.1.3, for $\theta_{\text{SiNR-CD-P}_\parallel} = 14 \pm 3^\circ$, the SiNR modified CD surface with parallel growth can also be viewed as a very rough hydrophilic surface. However, there are some differences compared to Fig.3.6. 1) Si NRs were also growing in the CD grooves in the parallel growth processing; 2) The nanorods tilted direction is parallel to the surface grooves in the way of nanorods parallel growth. A sketch of the morphology differences can be seen in Fig. 3.7.

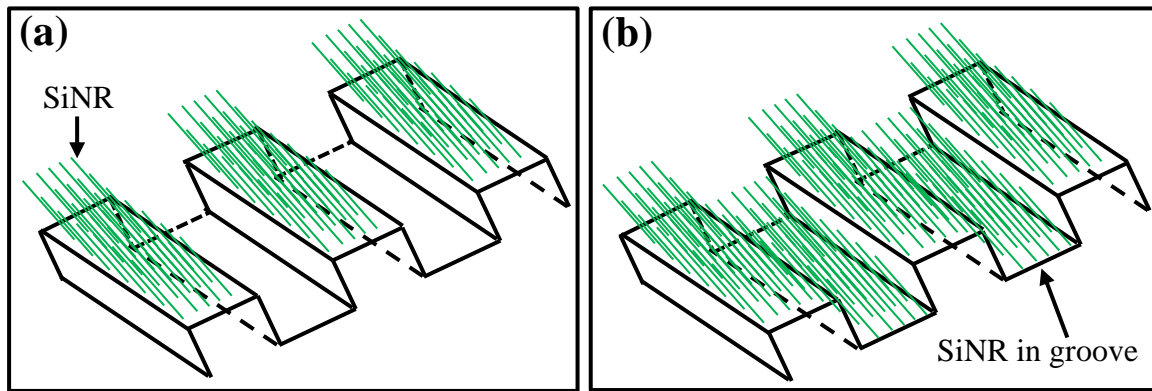


Figure 3.7. A sketch of surface morphology comparison for SiNR growing. (a) \perp surface grooves and (b) \parallel surface grooves.

Then, we can treat the SiNR modified CD substrate as a hydrophilic porous surface. A hemi-wicking theory can be used to model the surface wetting behavior. We can treat both nanorods on ridges and inside grooves are bundled together as shown in Fig.3.8.

Similar to the section 3.2.1.3, we can also apply the classic Cassie's law again to

predict $\theta_{\text{SiNR-CD-P}_{\parallel}}$ in this special case. The apparent contact angle $\theta_{\text{SiNR-CD-P}_{\parallel}}$ could also be determined by equation 3.7.

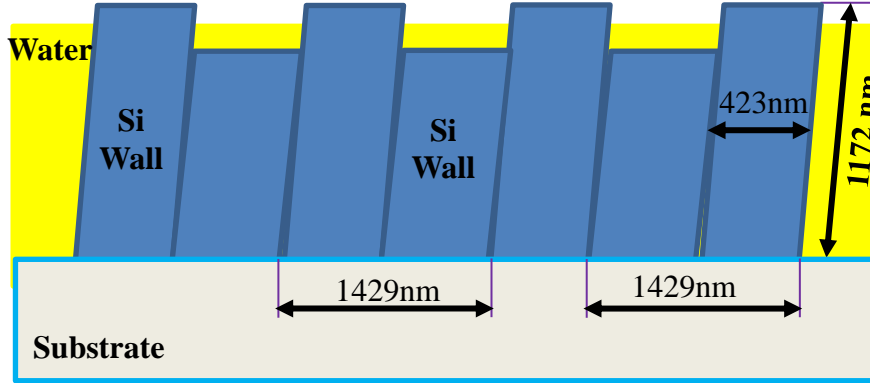


Figure 3.8. A morphological model of SiNR on CD substrate with parallel growth.

From section 3.2.1.3, when the water droplet achieves equilibrium after spreading, the water surface area fraction on the sample with SiNR parallel growth, as the sketch indicated in figure 3.6, could also be estimated by equation 3.7, which gave us a value of 0.704. This theoretical result obtained from SEM images is well consistent with the experimental result that the surface area fraction occupied by water in this silicon nanorod parallel growth case should be $f_{\text{H}_2\text{O}} = 0.72 \pm 0.7$.

However, similar with the description in section 3.2.1.3, a greater contact angle $\theta_{\text{SiNR-CD-P}_{\parallel}} = 14 \pm 3^\circ$ is measured when the drop is viewed from the direction parallel to the grooves compared with that measured in the perpendicular direction $\theta_{\text{SiNR-CD-P}_{\perp}} = 13 \pm 2^\circ$.

The contact angle difference ($\theta_{\parallel} - \theta_{\perp}$) is about 1° for the SiNR parallel growth sample, and this contact angle difference is much smaller than that for the SiNR vertical growth sample, which is about 9.2° . This is caused by the surface morphology differences between these two samples. Specifically speaking, there are some nanorod growing into the CD grooves for the parallel growth samples, however, the nanorods can only be deposited onto the ridges in the way of vertical growth due to the shadowing effect in Oblique Angle Deposition, as it can be seen

from the figure 3.4, 3.5 and 3.6. The following analysis might throw some light on this phenomenon.

As regarding of the Si nanorods fabricated with OAD at 86° vapor incident angle, they had a tilting angle of $51 \pm 3^\circ$ with respect to the substrate normal (Fan, et al. 2008). Then for our QCM reading 2000nm tilted silicon nanorods, the nanorod length is about 1172nm, and thus the nanorods vertical height is about 885nm, which is much larger than the groove depth 187nm. For our sample of silicon nanorod parallel growth on the CD substrate, the nanorods growing in the surface grooves will fill it up. When we deposit a droplet of water onto the surface, the nanaocarpet effect will make the tilted nanorod to form silicon walls, as can be seen in figure 3.8. Then the anisotropy of the surface morphology is reduced by the filled silicon nanorods, compared with the silicon nanorods vertical growth on the CD substrate. Then, this topographical structure anisotropy caused anisotropic wetting is undermined.

3.2.2 Watermark and Droplet Shape Discussion

The anisotropic wetting is reflected by the water droplet spreading shape. For a flat and homogeneous surface, the water droplet contour should be a circular shape as shown in Table 3.1. For the anisotropic surfaces, the droplet shape will be elongated. As shown in Table 3.2, the droplet shape on stripped CD surface has an aspect ratio $\eta = 1.17$; For the silicon thin film coated CD surface, $\eta = 1.19$; For Si nanorod coated CD surface, the aspect ratio η values are different depending on the coating method. For the parallel coating sample, $\eta = 1.08$, while for the perpendicular coating as shown in Table 3.2, the watermark becomes highly elongated along the surface grooves, and $\eta = 4.57$. Such an elongated anisotropic behavior on the silicon nanorod deposited CD samples can be explained by the so-called free energy barrier (FEB) theory. There are FEB distribution difference in different directions on the grooved structure due

to the geometrical and chemical inhomogeneities. There are more FEBs in the directions of perpendicular to the surface grooves.

Consequently, the three-phase contact line of the liquid was pinned perpendicular to the grooves and spreading along the grooves on the anisotropic samples surface, thus resulting in an asymmetric droplet shape (Long, et al. 2005; Morita, et al. 2005; Zhao, et al. 2007; Chung, et al. 2007; Li, et al. 2008; Yang, et al. 2009; Khare, et al. 2009). Detailed discussion could refer to the Appendix B.

3.3 CONCLUSION

In this chapter, we have experimentally studied the hydrophilic wetting properties of the engineered nanostructured surfaces. The experimental results indicate that the Si NRs deposited perpendicularly on CD substrates has demonstrated a significantly enhanced anisotropic wetting behavior. The shape of water droplet on this surface has an aspect ratio of 4.57, and the contact angle has an anisotropy with $\theta_{\perp} = 6.8 \pm 0.5^{\circ}$ and $\theta_{\parallel} = 16 \pm 2^{\circ}$. The contact angle on these rough surfaces can be explained by either classic Cassie's law or Wenzel's law.

Our results reveal that (1) the difference in the wetting behavior in the two directions is attributed to the anisotropic and highly directional surface features; (2) the high contact angle perpendicular to the groove direction is due to pinning of the contact line; (3) the low contact angle parallel to the groove direction is a result of preferential spreading of the droplet along the grooves due to roughness enhanced wetting.

CHAPTER 4

HYDROPHOBIC ANISOTROPIC WETTING

By modifying the silicon surface with HFTS, the surface will become hydrophobic. How would the hydrophobicity change as the surface morphology change is a very interesting problem, and we focus on answering this question in this chapter.

4.1 EXPERIMENTAL RESULTS

The experimental results of chapter 4 could be found in Table 4.1 and Table 4.2.

4.2 DATA INTERPRETATION AND DISCUSSION

4.2.1 Static Wetting Study and Comparison

4.2.1.1. Silicon thin film modified Silicon wafer vs. SiNR modified Si wafer

Silicon thin film modified silicon wafer after HFTS treatment: $\tilde{\theta}_{\text{Si}} = 118.3 \pm 0.3^\circ$, the Si nanorod modified silicon wafer: $\tilde{\theta}_{\text{SiNR-X}} = 141.5 \pm 0.3^\circ$ (CCD \perp VID) and $\tilde{\theta}_{\text{SiNR-Y}} = 139.6 \pm 0.5^\circ$ (CCD \parallel VID)

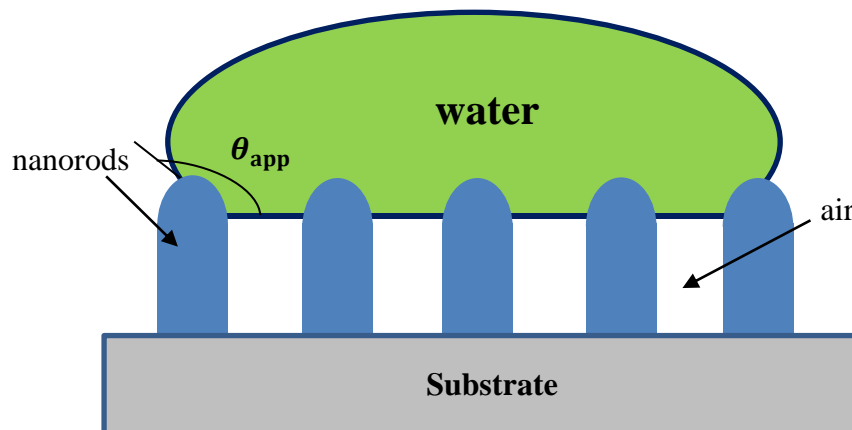


Figure 4.1. A sketch of the water droplet resting on hydrophobic silicon nanorods surfaces.

Table 4.1 Static Contact Angle Measurement on Si thin film modified surface with HFTS treatment

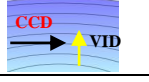
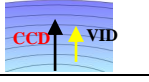
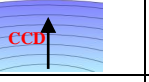
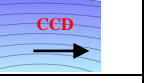


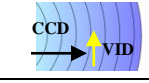
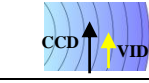
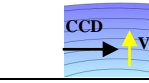
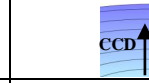
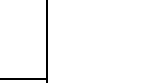




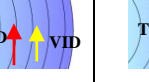
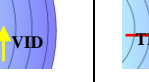
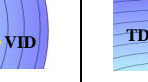
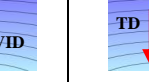
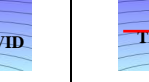
Chemical Treatment	Silicon Wafer		CD Substrate			
	Si Wafer as a control	Si thin film Modified	Si Modified	Si Modified	Bared CD	Bared CD
Without HFTS	$28.5 \pm 0.5^\circ$	$28 \pm 1^\circ$				
HFTS Treated	$114 \pm 1^\circ$	$118.3 \pm 0.3^\circ$	$128.5 \pm 0.6^\circ$	$124.8 \pm 0.5^\circ$	–	–

Table 4.2 Static Contact Angle Measurement on SiNR Modified Surface after HFTS Treatment

After Si thin film modification, QCM reading 2000nm SiNR will be grown onto CD or Si wafer <i>via</i> OAD at 86° vapor incident angle								
Substrate	Si Wafer			CD Substrate				
Chemical Treatment	SiNR modified	SiNR modified	SiNR modified	SiNR Modified	SiNR Modified	SiNR Modified	SiNR Modified	SiNR Modified
Without HFTS								
HFTS Treated	$10.8 \pm 0.6^\circ$	$9.7 \pm 0.9^\circ$	$13 \pm 2^\circ$	$14 \pm 3^\circ$	$16 \pm 2^\circ$	$6.8 \pm 0.5^\circ$	$141.5 \pm 0.3^\circ$	$139.6 \pm 0.5^\circ$
Sliding Angle								
	$77 \pm 4^\circ$	$46 \pm 1^\circ$	$51 \pm 2^\circ$	$71 \pm 7^\circ$	$34 \pm 3^\circ$	$45 \pm 2^\circ$	$49 \pm 2^\circ$	$23 \pm 1^\circ$

Annotation for table 4.1 and 4.2:

1. CCD : The center line of CCD (Data Physics OCA 20) when we measure the static contact angle by the sessile drop method with a fixed 2 μ L water droplet.
2. VID : The Vapor Incident Direction when we fabricated nanorod by the OAD method using a custom-designed electron-beam evaporation system.
3. TD: The sample tilted direction when we measure the sliding angle with a fixed 10 μ L water droplet.

After the HFTS treatment, the deposited DI water rest on the sample surface in a Cassie's state as can be seen in Fig. 4.1, and the water can only wet the tips of the nanorods for the high aspect ratio hydrophobic surfaces (Fan, et al. 2004). Therefore, the water droplet was in fact spreading along a composite Si-air surfaces. According to the Cassie' law, the apparent contact angle of HFTS treated Si NRs modified Si wafer can be expressed as,

$$\cos \tilde{\theta}_{\text{SiNR}} = f_{\text{SiNR}} \cdot \cos \tilde{\theta}_{\text{Si}} + f_{\text{SiNR}} - 1, \quad (4.1)$$

where f_{SiNR} denote the fraction of silicon nanorods underneath the DI water droplet.

Using the contact angles we obtained, we can get $f_{\text{SiNR}} = 0.43 \pm 0.03$. This result is well consistent with the theoretical nanorods coverage $f'_{\text{SiNR}} = 0.43$ estimated by ImageTool with the top view SEM image (Fan, et al. 2004).

4.2.1.2. Silicon thin film modified Silicon wafer vs. Silicon thin film modified CD substrate

The contact angle of Si thin film coated silicon wafer: $\tilde{\theta}_{\text{Si-CD-}\parallel} = 128.5 \pm 0.6^\circ$ (CCD \parallel Groove) and $\tilde{\theta}_{\text{Si-CD-}\perp} = 124.8 \pm 0.5^\circ$ (CCD \perp Groove).

Similar to Si NR case, after the HFTS treatment, the water rests on the sample surface in a Cassie's state, and the apparent contact angle is determined by,

$$\cos \tilde{\theta}_{\text{Si-CD}} = f_{\text{Si-CD}} \cdot \cos \tilde{\theta}_{\text{Si}} + f_{\text{Si-CD}} - 1, \quad (4.2)$$

where $f_{\text{Si-CD}}$ denotes the fraction of silicon surface underneath the DI water droplet, according to Cassie's law. Using the contact angles obtained, we can get $f_{\text{Si-CD}} = 0.72 \pm 0.02$.

Based on the AFM top-view of the CD surface and also its corresponding section analysis, as can be seen in figure 4.2, we can roughly obtain the morphology parameters of the CD surface: width of the ridge: $W_R = 0.83 \pm 0.03 \mu\text{m}$, and also the width of groove: $W_G = 0.34 \pm 0.02 \mu\text{m}$. Thus, theoretically, the fraction of silicon surface underneath the DI water droplet can be written as:

$$f'_{\text{Si-CD}} = W_{\text{R}}/W_{\text{R}} + W_{\text{G}} = 0.71. \quad (4.3)$$

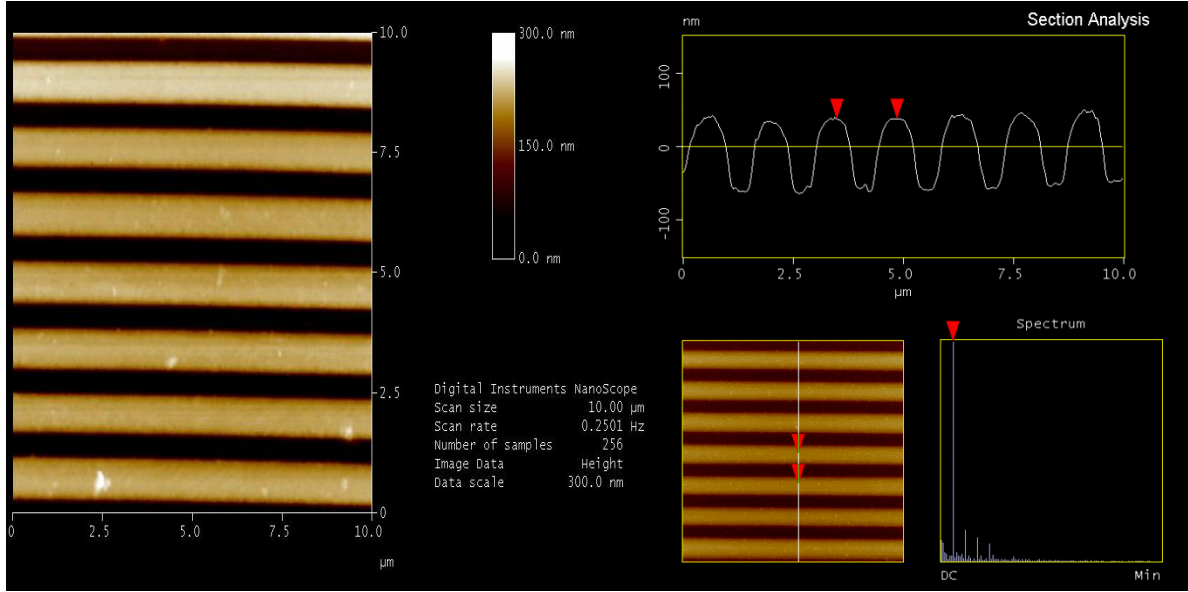


Figure 4.2. An AFM characterization of the polymer-stripped-off CD surface. Top view of $10 \times 10 \mu\text{m}^2$ topographic image and also its corresponding section analysis data. The AFM pictures analysis is carried out with the Nanoscope Control Software (Quadrex, Digital Instrument).

We can see that there is a slight difference between the experimental and theoretical results of the fraction of silicon surface underneath the DI water droplet. There is a possibility of for this inconsistency. Specifically, from the section analysis part, we can get to know that the ridge of the CD surface is not smooth, that is to say, actual width of the ridge W_{R} should be larger than the value $0.83 \pm 0.03 \mu\text{m}$ obtained from equation 4.3. Thus, the theoretic fraction of silicon surface underneath the DI water droplet should be slightly larger than 0.71.

4.2.1.3 Silicon thin film modified Silicon wafer vs. SiNR vertical growth on CD substrate

The contact angle of SiNR vertical growth on CD substrate after HFTS treatment is $\tilde{\theta}_{\text{SiNR-CD-V}_{\parallel}} = 145 \pm 1^\circ$ and $\tilde{\theta}_{\text{SiNR-CD-V}_{\perp}} = 140.7 \pm 0.3^\circ$.

For this particular case, since the surface has both the groove and nanorod structure, the

water droplet will reside on the groove modified NR surfaces as shown in Fig.4.3. According to Cassie's law, the fraction of SiNR on the surface can be experimentally obtained. Such a surface can be treated as CD groove modulated Si nanorod surface. Theoretically, $f'_{\text{SiNR-CD-V}}$ can be written as:

$$f'_{\text{SiNR-CD-V}} = f'_{\text{Si-CD}} \cdot f'_{\text{SiNR}} \quad (4.4)$$

where $f'_{\text{Si-CD}}$ is the theoretical fraction of silicon surface for CD substrate, and f'_{SiNR} is the theoretical fraction of silicon surface for silicon nanorods.

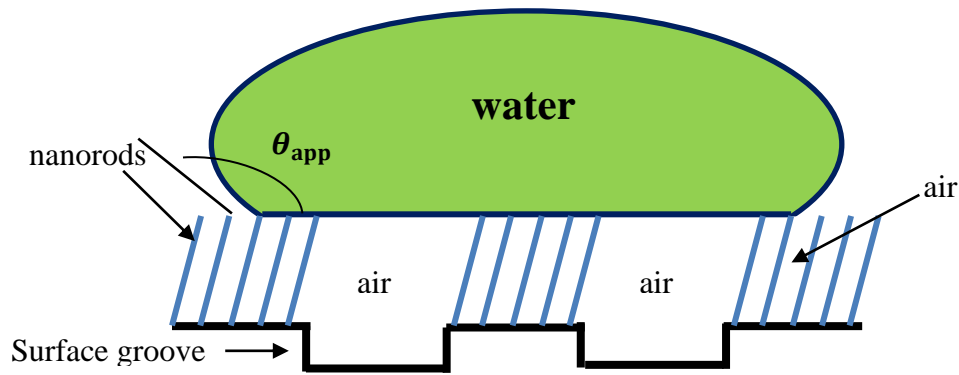


Figure 4. 3. A sketch of the cross-sectional view of the water droplet resting on the sample of the SiNR vertical growth on CD substrate in a Cassie's state.

From above two sections, we have $f'_{\text{Si-CD}} = 0.71$ and $f'_{\text{SiNR}} = 0.43$. Therefore, the predicted $f'_{\text{SiNR-CD-V}}$ is 0.31. And this value is consistent with the experimentally obtained value.

4.2.1.4 Silicon thin film modified Silicon wafer vs. SiNR parallel growth on CD substrate

The static contact angles of SiNR parallel growth on CD substrate with HFTS treatment are $\tilde{\theta}_{\text{SiNR-CD-P}_{\parallel}} = 142.2 \pm 0.4^{\circ}$ (CCD \parallel Groove) and $\tilde{\theta}_{\text{SiNR-CD-P}_{\perp}} = 141.7 \pm 0.9^{\circ}$ (CCD \perp Groove).

For this surface, the DI water rests on the sample surface in a Cassie's state, as shown in

Fig. 4.4. According to Cassie's law, one can obtain experimentally that $f_{\text{SiNR-CD-P}} = 0.41 \pm 0.02$. This solid fraction is approximately equal to the solid fraction of the silicon nanorods growing on the silicon wafer, which is 0.43 estimated by ImageTool (Fan, et al. 2004).

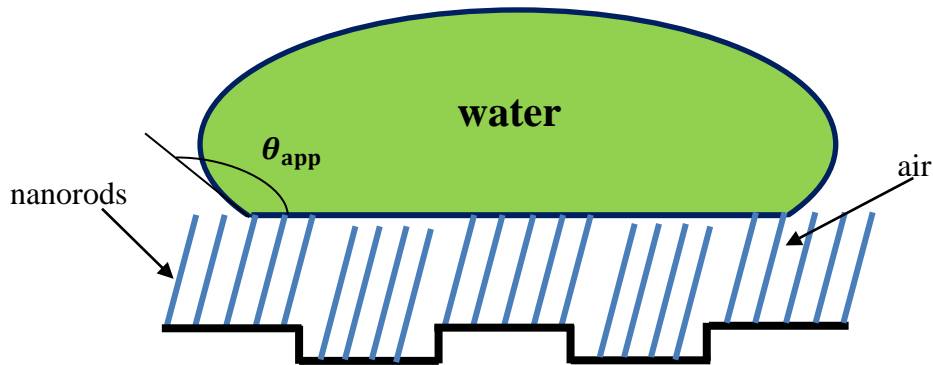


Figure 4.4. A sketch of the cross-sectional view of the water droplet resting on the sample of the SiNR parallel growth on CD substrate in a Cassie's state.













4.2.2 Sliding angle

For hydrophobic surfaces, sliding angle characterization is very important. Table 4.3 summarized the sliding angle measurements for all surface we have.

We can see a general trend: the sliding angle of SiNR modified CD surface is smaller than the plane SiNR surfaces. The SiNR \perp CD surface has a smaller sliding angle than that SiNR \parallel CD. This also correspond to the contact angle: larger contact angle has smaller sliding angle. Since all the droplets are in Cassie's state, the larger the contact angle, the smaller the surface fraction of silicon get contacted, the less pinning effect for sliding. So the sliding angle become smaller.

Another trend is that the direction of SiNR affects the sliding angle. For the same surface, the sliding angle along the Si NR tilted direction is smaller than that against NR tilting direction. This is because of the larger pinning effect when water droplet slides against NR tilted direction. Detailed analysis could be found in appendix C.

Table 4.3.Sliding Angle Measurement for SiNR Modified Samples

Samples	Sliding Angle (°)	
SiNR modified Si wafer 		77 ± 4°
		46 ± 1°
		51 ± 2°
SiNR modified CD Substrate with parallel Growth 		71 ± 7°
		34 ± 3°
		45 ± 2°
SiNR modified CD Substrate with vertical Growth 		49 ± 2°
		23 ± 1°
		25 ± 2°

*Table annotation: **VID** : The Vapor Incident Direction when we fabricated nanorod by the OAD method using a custom-designed electron-beam evaporation system. **TD**: The sample tilted direction when we measure the sliding angle with a fixed 10 μL water droplet.

4.3 CONCLUSION

Modified the engineering surfaces with HFTS to make them hydrophobic. Both the contact angle and sliding angle of those surface were measured and compared. We found that the contact angle results could be well explained by the classical Cassie’s law, with both the experimentally determined and theoretically estimated surface fraction agree with each other very well. The

sliding angle of the surfaces depends on the surface fraction as well as the sliding direction with respect to the nanorods tilted directions.

CHAPTER 5

CONCLUSION AND FUTURE WORK

In this thesis, we report the wetting properties of engineered nanofilms, composed of an array of titled Si Nanorods growing onto the compact disk surface by means of oblique angle deposition. We have shown that the SiNR \perp CD surface shows a significantly enhanced anisotropic wetting behavior.

For the hydrophilic films, Si NRs deposited perpendicularly on CD substrates has demonstrated a significantly enhanced anisotropic wetting behavior. The shape of water droplet on this surface has an aspect ratio of 4.57, and the contact angle has an anisotropy with $\theta_{\perp}=6.8\pm 0.5^{\circ}$ and $\theta_{\parallel}=16\pm 2^{\circ}$. The contact angle on these rough surfaces can be explained by either classic Cassie's law or Wenzel's law.

For the hydrophobic surface treated by HF-TS, the contact angle results could be well explained by the classical Cassie's law, with both the experimentally determined and theoretically estimated surface fraction agree with each other very well. The sliding angle of the surfaces depends on the surface fraction as well as the sliding direction with respect to the nanorods tilted directions.

In the future, it will be of great interest to enhance wetting anisotropy by further engineering the surface both theoretically and experimentally. Although the concept of energy barrier is "of utmost importance in determining hysteresis" (Johnson and Dettre. 1964) and has found practical applications, existing theoretical studies on energy barriers are very limited. Most studies provided only qualitative discussion about the effect of energy barriers on contact angle

phenomena for anisotropic wetting study. A quantitative correlation between surface geometrical parameters and contact angles and a thorough mechanism responsible for this effect of textures are lacking.

Experimentally, anisotropic wetting on chemically or physically patterned structures has been studied using micrometer-scale features due to technical limitations, there has been few deliberate efforts to demonstrate whether sub-micrometric, or smaller, features would also lead to the macroscopic distortion of water drops , and how this would occur. This remains a challenge in this field.

REFERENCES

- Abott, N. L., Folkers, J. P., Whitesides, G. M. Manipulation of the wettability of surfaces on the 0.1-1-micrometer scale through micromachining and molecular self-assembly. *Science* **1992**, 257, 1380-1382.
- Alvine, K. J.; Shpyrko, O. G.; Pershan, P.S.; Shin, K.; Russell T.P.; Capillary filling of anodized alumina nanopore arrays. *Phys. Rev Lett.* **2006**, 97, 175503
- Azzam, R. M.; Chiral thin solid films: Method of deposition and applications, *Appl. Phys. Lett.* **1992**, 61, 3118–3120.
- Bico, J., Tordeux, C. and Quéré D. Rough wetting. *Europhys. Lett.* **1999**, 55, 214-220.
- Bico, J.; Thiele, U. and Quere, D. ; Wetting of textured surfaces. *Colloid Surf. A*, **2002**, 206, 41-46.
- Bico, J.; Marzolin, C.; Quéré D. Pearl drops. *Europhysics Letters*, **1999**, 47, 220-226
- Bliznyuk, O.; Vereshchagina, E.; Stefan Kooij, E.; Poelsema, B. Scaling of anisotropic droplet shapes on chemically stripe-patterned surfaces. *Physical Review E*. **2009**, 79, 041601.
- Blossey, R. Self-cleaning surfaces — virtual realities. *Nature Material* **2003**, 2, 301–306.
- Brandon, S.; Haimovich, N.; Yegar, E.; Marmur, A. Partial wetting of chemically patterned surfaces: The effect of drop size. *J. Colloid Interface Sci.* **2003**, 263, 237.
- Brown, J. F. Laboratory vessel having hydrophobic coating and process for manufacturing same. U.S. Patent 5,853,894, Issued December 29, 1998.
- Bruschi, L.; Carlin, A.; Parry, A.O. and G. Mistura, Crossover effects in the wetting of adsorbed films in linear wedges, *Phys. Rev. E*. **2003**, 68, 021606
- Bush, J. W. M., Hu, D. L. & Prakash, M. The integument of water-walking arthropods: Form and function. *Adv. Insect Physiol.* **2007**, 34, 117-192.
- Calvert, J. M. Lithographic patterning of self-assembled films. *J. Vac. Sci. Technol. B*. **1993**, 11, 2155-2163.
- Cassie, A.B.D; Baxter, S. Wettability of Porous Surfaces. *Trans. Faraday Soc.* **1944**, 40, 546–551
- Cebeci, F. Ç., Wu, Z., Zhai, L., Cohen, R. E. & Rubner, M. F. Nanoporosity-driven superhydrophi-

- licity: A means to create multifunctional antifogging coatings. *Langmuir* **2006**, *22*, 2856-2862.
- Chaney, S. B.; Shanmukh, S.; Dluhy, R. A. and Zhao, Y. P.; Aligned silver nanorod arrays produce high sensitivity surface-enhanced Raman spectroscopy substrates. *Appl. Phys. Lett.* **2005**, *87*, 031908–031903
- Checco, A.; Gang, O. ; Ocko, B.M.; Liquid nanostripes. *Phys. Rev. Lett.* **2006**, *96*, 056104.
- Chen, Y., He, B., Lee, J. & Patankar, N. A. Anisotropy in the wetting of rough surfaces. *J. Colloid Interface Sci.* **2005**, *281*, 458-464.
- Cheng, Y. T., Rodak, D. E. Is the lotus leaf superhydrophobic? . *Appl. Phys. Lett.* **2005**, *86*, 144101-144103.
- Chiou, N.-R., Lu, C., Guan, J., Lee, L. J. & Epstein, A. J. Growth and alignment of polyaniline nanofibres with superhydrophobic, superhydrophilic and other properties. *Nature Nanotechnology.* **2007**, *2*, 354-357.
- Chou, S. Y.; Krauss, P. R.; Renstrom, P. Imprint of sub-25 nm vias and trenches in polymers. *J. Appl. Phys. Lett.* **1995**, *67*, 3114-3116.
- Chu, K. H., Xiao, R. & Wang, E. N. Uni-directional liquid spreading on asymmetric nanostructured surfaces. *Nature Material.* **2010**, *9*, 413-417.
- Chung, J. Y., Youngblood, J. P. & Stafford, C. M. Anisotropic wetting on tunable micro-wrinkled surfaces. *Soft Matter.* **2007**, *3*, 1163-1169.
- Courbin, L. et al. Imbibition by polygonal spreading on microdecorated surfaces. *Nature Material.* **2007**, *6*, 661-664.
- de Gennes, P. G. Wetting: statics and dynamics. *Rev. Mod. Phys.* **1985**, *57*, 827–863.
- Drelich, J. and Chibowski, E. Superhydrophilic and Superwetting Surfaces: Definition and Mechanisms of Control. *Langmuir* **2010**, *26*, 18621–18623.
- Drelich, J.; Wilbur, J. L.; Miller, J. D.; Whitesides, G. M. Contact Angles for Liquid Drops at a Model Heterogeneous Surface Consisting of Alternating and Parallel Hydrophobic/Hydrophilic Strips. *Langmuir* **1996**, *12*, 1913–1922.
- Driskell, J.; Shanmukh, S.; Liu, Y.; Chaney, S.; Tang, X.-J.; Zhao, Y.-P. and Dluhy, R.; The use of aligned silver nanorod arrays prepared by oblique angle vapor deposition, *J. Phys. Chem. C*, **2008**, *112*, 895–901.
- Dupuis, A., L'époldès, J., Bucknall, D. G. & Yeomans, J. M. Control of drop positioning using

- chemical patterning. *Appl. Phys. Lett.* **2005**, 87, 024103.
- Dussan V., E. B. *J. Fluid Mech.* **1985**, 151,1-20
- Evans, S. D., Flynn, T. M. and Ulman, A. Self-assembled multilayer formation on prede®ned templates. *Langmuir* **1995**, 11, 3811-3814.
- Extrand, C. W. Retention forces of a liquid slug in a rough capillary tube with symmetric or asymmetric features. *Langmuir* **2007**, 23, 1867-1871.
- Extrand, C. W., Moon, S. I., Hall, P. & Schmidt, D. Superwetting of structured surfaces. *Langmuir* **2007**, 23, 8882-8890.
- Fan, J. G. and Zhao, Y. P. Characterization of watermarks formed in nano-carpet effect. *Langmuir* **2006**, 22, 3662–3671.
- Fan, J. G. and Zhao, Y. P.; Spreading of a Water Droplet on a Vertically Aligned Si Nanorod Array, *Appl. Phys. Lett.* **2007**, 90, 013102.
- Fan, J. G.; Dyer, D.; Zhang, G. G. and Zhao, Y. P. Nano-carpet effect: pattern formation during the wetting of vertically aligned nanorod array. *Nano Letters* **2004**, 4, 2133–2138.
- Fan, J. G.; Fu, J. X.; Collins, A. and Y-P Zhao, The effect of the shape of nanorod arrays on the nanocarpet effect, *Nanotechnology* **2008**,19, 045713.
- Fan, J. G.; Tang, X. J. ; Zhao, Y. P. ; Water contact angles of vertically aligned Si nanorod arrays , *Nanotechnology* **2004**, 15, 501–504.
- Feng, X.; Jiang, L. Design and Creation of Superwetting/Antiwetting Surfaces. *Advance Material* **2006**, 18, 3063.
- Fujishima, A.; Rao, T. N.; Tryk, D. A. TiO₂ photocatalysts and diamond electrodes. *Electrochim. Acta* **2000**, 45, 4683-4690.
- Gang, O.; Alvine, K. J.; Fukuto, M.; Pershan, P. S.; Black, C. T.; Ocko, B. M. Liquids on topologically nano-patterned surfaces , *Phys. Rev. Lett.* **2005**, 95, 217801
- Gao, X. F.; Yao, X.; Jiang, L.; Effects of Rugged Nanoprotrusions on the Surface Hydrophobicity and Water Adhesion of Anisotropic Micropatterns. *Langmuir* **2007**, 23, 4886–4891.
- Garrod, R. P. et al. Mimicking a stenocara beetle's back for microcondensation using plasmachemical patterned superhydrophobic-superhydrophilic surfaces. *Langmuir* **2007**, 23, 689-693
- Gau, H.; Herminghaus, S.; Lenz, P.; Lipowsky, R. Liquid Morphologies on Structured Surfaces:

- From Microchannels to Microchips. *Science* **1999**, 283, 5398 ,46-49.
- Gleiche, M., Chi, L. F. & Fuchs, H. Nanoscopic channel lattices with controlled anisotropic wetting. *Nature* **2000**, 403, 173-175.
- Gleiche, M.; Chi, L.; Gedig, E.; Fuchs, H. Anisotropic Contact-Angle Hysteresis of Chemically Nanostructured Surfaces, *ChemPhysChem* **2001**, 2, 187-191.
- Grunze, M. Driven liquids. *Science* **1999**. 283, 41-42.
- Hiratsuka, K., Bohno, A. & Endo, H. Water droplet lubrication between hydrophilic and hydrophobic surfaces. *J. Phys. Conf. Ser.* **2007**, 89, 012012.
- Hofmann, T.; Tasinkevych, M.; Checco, A.; Dobisz, E.; Dietrich, S.; Ocko, B. M. Wetting of Nanopatterned Grooved Surface. *Physical Review Letters* **2010**, 104, 106102.
- Huber, G. et al. Evidence for capillarity contributions to gecko adhesion from single spatula nanomechanical measurements. *Proc. Natl Acad. Sci. USA* **2005**, 102, 16293-16296.
- Johnson, R.E.; Dettre R. H.; Contact Angle Hysteresis I. Study of an Idealized Rough Surface. *Adv Chem Ser* **1964**, 43, 112-135.
- Katsunori Y. and Masamichi I.; Recent progress in environmental catalytic technology. *Chemistry and Materials Science*. **2000**, 4, 83-90.
- Khare, K. ; Zhou, J. H.; Yang, S.; Tunable Open-Channel Microfluidics on Soft Poly(dimethylsiloxane) (PDMS) Substrates with Sinusoidal Grooves. *Langmuir*. **2009**, 25, 12794–12799.
- Kityk, A.V; Hofmann, T.; Knorr, K.; Liquid-vapor coexistence at a mesoporous substrate. *Phys Rev Lett*. **2008**, 100, 036105
- Koch, K.; Bhushan, B. & Barthlott, W. Diversity of structure, Morphology and Wetting of Plant Surfaces. *Soft matter*. *Soft Matter*, **2008** , 4, 1943-1950.
- Krupenkin, T. N., Taylor, J. A., Schneider, T. M. & Yang, S. From rolling ball to complete wetting: The dynamic tuning of liquid on nanostructured surfaces. *Langmuir* **2004**, 20, 3824-3827.
- Kumar, A.; Biebuyck, H. A.; Whitesides G. M.; Patterning Self-Assembled Monolayers: Applications in Materials Science. *Langmuir* **1994**, 10, 1498–1511.
- Kusumaatmaja, H., Vrancken, R. J., Bastiaansen, C. W. M. & Yeomans, J. M. Anisotropic drop morphologies on corrugated surfaces. *Langmuir* **2008**, 24, 7299-7308.
- Li, D., Neumann, A. W., Surface heterogeneity and contact angle hysteresis. *Colloid Polym Sci*.

1992, 270, 498-504.

- Li, W.; Amirfazli, A.; A thermodynamic approach for determining the contact angle hysteresis for superhydrophobic surfaces. *J. of Colloid and Interface Sci.* **2005**, 292, 195–201.
- Li, W.; Fang, G. P.; Li, Y.F.; Qiao, G.J. Anisotropic Wetting Behavior Arising from Superhydrophobic Surfaces: Parallel Grooved Structure. *J. Phys.Chem.B.* **2008**, 112, 7234-7243.
- Linke, H. et al. Self-propelled Leidenfrost droplets. *Phys. Rev. Lett.* **2006**, 96, 154502.
- Liu, F.; Umlor, M.T.; Shen, L.; Weston, J.; Eads, W.; Barnard, J.A.; Mankey, G. J. The growth of nanoscale structured iron films by glancing angle deposition. *J. Appl. Phys.* **1999**, 85, 5486-5488.
- Liu, Y. J.; Chu, H. and Zhao, Y.P.; Silver nanorod array substrates fabricated by oblique angle deposition: morphological, optical and SERS characterizations. *J. Phys. Chem. C* **2010**, 114, 8176–8183.
- Lloyd, T. B., Connelly, G.M.; Direct measurement of energy barriers on rough and heterogeneous solid surfaces. *J. Adhes* **1997**, 63, 141-151.
- Long, J.; Chen, P.; On the role of energy barriers in determining contact angle hysteresis. *Advances in Colloid and Interface Science* **2006**, 127, 55–66.
- Long, J.; Hyder, M. N.; Huang, R. Y. M.; Chen, P. Thermodynamic modeling of contact angles on rough, heterogeneous surfaces. *Advances in Colloid and Interface Science* **2005** , 118, 173 – 190.
- Ma, M.; Hill, R.M.; Current Opinion in Colloid and Interface. *Science* **2006**, 11, 193-202.
- Mahdavi, A. et al. A biodegradable and biocompatible gecko-inspired tissue adhesive. *Proc. Natl Acad. Sci. USA* **2008**, 105, 2307-2312.
- Malvadkar, N. A.; Hancock, M. J.; Sekeroglu, K., Dressick, W. J.; Demirel, M. C. An engineered anisotropic nanofilm with unidirectional wetting properties, *Nature Materials* **2010**, 9, 1023–1028.
- Maritines, E. et al. Superhydrophobicity and super hydrophilicity of regular nanopatterns. *Nano Lett.* **2005**, 5, 2097-2130.
- Marmur, A., Wetting on Hydrophobic Rough Surfaces: to be Heterogeneous or not to be?, *Langmuir* **2003**, 19, 8343-8348.
- Marmur, A.; Contact angle hysteresis on heterogeneous smooth surfaces. *J. Colloid Interface Sci.*

1994,168, 40-49.

Martines, E.; Seunarine, K.; Morgan, H.; Gadegaard, N.; Wilkinson, C. D. W. ; Riehle, M. O. Superhydrophobicity and Superhydrophilicity of Regular Nanopatterns. *Nano Letters* **2005**, 5, 2097-2103.

Meng N. C.; Bo J.; Christopher W. K. C.; Chris S.; *Water Research* **2010**. 44, 2997-3027.

Messier, R.; Venugopal, V. C.; Sunal, P.D.; Origin and evolution of sculptured thin films. *J. Vac. Sci. Technol. A.* **2000**, 18, 1538–1545.

Miwa, M; Nakajima, A.; Fujishima, A.; Hashimoto, K.; Watanabe, T. Effects of the Surface Roughness on Sliding Angles of Water Droplets on Superhydrophobic Surfaces. *Langmuir* **2000**, 16, 5754–5760.

Morita, M.; Koga, T.; Otsuka, H.; Takahara, A. Macroscopic-Wetting Anisotropy on the Line-Patterned Surface of Fluoroalkylsilane Monolayers. *Langmuir* **2005**, 21, 911-918.

Motohiro, T. and Taga, Y. Thin film retardation plate by oblique deposition, *Appl. Opt.* **1989**, 28, 2466–2482.

Narhe, R. D., Beysens, D. A. Water condensation on a super-hydrophobic spike surface. *Europhys. Lett.* **2006**, 75, 98–104.

Neumann, A. W.; Good, R. J. Thermodynamics of contact angles I. Heterogeneous solid surfaces. *J. Colloid Interface Sci.* **1972**, 38, 341.

Neumann, A.W. Contact angles and their temperature dependence: thermodynamic status, measurement, interpretation and application. *Advances in Colloid and Interface Science* **1974**, 4, 105-191.

Oelschlägel, B., Gorb, S., Wanke, S. & Neinhuis, C. Structure and biomechanics of trapping flower trichomes and their role in the pollination biology of Aristolochia plants (Aristolochiaceae). *New Phytol.* **2009**, 184, 988-1002.

Onda, T.; Shibuichi, S.; Satoh, N.; Tsujii, K. Super-Water-Repellent Fractal Surfaces. *Langmuir* **1996**, 12, 2125–2127.

Oner, D. and McCarthy, T. J. Ultrahydrophobic surfaces. Effects of topography length scales on wettability. *Langmuir* **2000**,16, 7777-7782.

Pesika, N. S. et al. Gecko adhesion pad: A smart surface? *J. Phys. Condens. Matter* **2009**, 21, 464132.

Prakash, M., Qu é é D. & Bush, J. W. M. Surface tension transport of prey by feeding shorebirds:

- the capillary ratchet. *Science* **2008**,320, 931- 934.
- Quéré D. Non-sticking drops. *Rep. Prog. Phys.* **2005**, 68, 2495-2532.
- R. J. Good, A thermodynamic derivation of Wenzel's modification of Young's equation, together with a theory of hysteresis, *J. Am. Chem. Soc.* **1953**,74, 5041-5043.
- Ren, T. B.; Feng, Y.; Dong H.Q.; Li L.; Li Y. Y.; Sheddable Nanoparticles for Biomedical Application. *Progress in Chemistry* **2011**, 23, 213-220
- Renvoisé P., Bush, J. W. M., Prakash, M. & Quéré D. Drop propulsion in tapered tubes. *Europhys. Lett.* **2009**, 86, 64003.
- Roach, P.; Shirtcliffe, N. J.; Newton, M. I. Progress in superhydrophobic surface development. *Soft Matter*, **2008**, 4, 224-240
- Robbie, K. and Brett, M. J.; Sculptured thin films and glancing angle deposition: Growth mechanics and applications. *J. Vac. Sci. Technol.* **1997**, A 15, 1460-1465.
- Robbie, K.; Brett, M. J.; Lakhtakia, A. Chiral sculptured thin films. *Nature (London)*. **1996**, 384, 616.
- Robbie, K.; Friedrich, L. J.; Dew, S. K.; Smy, T.; Brett, M. J. Fabrication of thin films with highly porous microstructures. *J. Vac. Sci. Technol.* **1995**, A 13, 1032-1035.
- Robbins, M. O., Andelman, D., and Joanny, J. F. Thin liquid films on rough or heterogeneous solids. *Phys. Rev.A.* **1991**, 43, 4344-4354.
- Sandre, O., Gorre-Talini, L., Ajdari, A., Prost, J. & Silberzan, P. Moving droplets on asymmetrically structured surfaces. *Phys. Rev. E.* **1999**, 60, 2964-2972.
- Schonhorn, H. Anisotropic Wetting of Liquids on Finely Grooved Surfaces. *J. Adhesion* **1987**, 23, 147-156.
- Seemann, R., Brinkmann, M., Kramer, E. J., Lange, F. F. & Lipowsky, R. Wetting morphologies at microstructured surfaces. *Proc. Natl Acad. Sci. USA* **2005**, 102, 1848-1852.
- Shastry, A., Case, M. J. & Böhinger, K. F. Directing droplets using microstructured surfaces. *Langmuir* **2006**, 22, 6161-6167.
- Shibuichi, S.; Onda, T.; Satoh, N.; Tsujii, K. Super Water-Repellent Surfaces Resulting from Fractal Structure. *J. Phys. Chem.*, **1996**, 100, 19512–19517.
- Shibuichi, S.; Yamamoto, T.; Onda, T.; Tsujii, K. Super Water- and Oil-Repellent Surfaces Resulting from Fractal Structure. *J. Colloid Interface Sci.* **1998**, 208, 287-294.
- Shirtcliffe, N.J.; McHale, G.; Newton, M. I.; Perry, C. C. Intrinsically superhydrophobic

- organosilica sol-gel foams. *Langmuir* **2003**, 19 , 5626–5631.
- Shuttleworth, A.R., Bailey, G.L.J.; The Spreading of a Liquid Over a rough Solid. *Discuss Faraday Soc.* **1948**, 3, 16-22.
- Tada, H.; Nagayama, H.; Chemical Vapor Surface Modification of Porous Glass with Fluoroalkyl-Functional Silanes. 1. Characterization of the Molecular Layer. *Langmuir* **1994**, 10, 1472–1476.
- Tait, R. N.; Smy, T.; Brett, M. J. Modelling and characterization of columnar growth in evaporated films. *Thin Solid Films* **1993**, 226, 196-201.
- Takeda, S.; Fukawa, M.; Hayashi, Y.; Matsumoto, K. Surface OH group governing adsorption properties of metal oxide films. *Thin Solid Films* **1999**, 339, 220-224.
- Takeda, S.; Yamamoto, K.; Hayasaka, Y.; Matsumoto, K. Surface OH group governing wettability of commercial glasses. *J. Non-Cryst. Solids* **1999**, 249, 41-46.
- Teare, D.O.H.; Spanos, C. G.; Ridley, P.; Kinmond, E. J.; Roucoules, V.; Badyal, J. P. S.; Brewer, S. A.; Coulson, S. et al. Pulsed plasma deposition of super-hydrophobic nanospheres. *Chemistry of Materials* **2002**, 14 ,4566–4571
- Vorobyev, A. Y. & Guo, C. Metal pumps liquid uphill. *Appl. Phys. Lett.* **2009**, 94, 224102.
- Wang, J. Z., Zheng, Z. H., Li, H. W., Huck, W. T. S. & Sirringhaus, H. Dewetting of conducting polymer inkjet droplets on patterned surfaces. *Nature Material.* **2004**, 3, 171-176.
- Wang, R. et al. Light induced amphiphilic surfaces. *Nature* **1997**, 388, 431-432.
- Wang, R.; Sakai, N.; Fujishima, A.; Watanabe, T.; Hashimoto, K. Studies of Surface Wettability Conversion on TiO₂ Single-Crystal Surfaces *J. Phys. Chem. B* **1999**, 103, 2188- 2194.
- Wenzel, R. N. Resistance of solid surfaces to wetting by water. *Ind. Eng. Chem.* **1936**, 28, 988-994
- Wittmann, J. C. and Smith, P. Highly oriented thin films of poly(tetrafluoroethylene) as a substrate for oriented growth of materials. *Nature* **1991**, 352, 414-417.
- Wolansky, G., and Marmur, A.; Apparent Contact Angles on Rough Surfaces: the Wenzel Equation Revisited, *Colloids and Surfaces A* **1999**, 156, 381-388.
- Wouters, D.; Schubert, U. S.; Nanolithography and Nanochemistry: Probe-Related Patterning Techniques and Chemical Modification for Nanometer-Sized Devices. *Angew. Chem., Int. Ed.* **2004**, 43, 2480–2495.
- Xia, D.Y.; Brueck, S. R. J. Strongly Anisotropic Wetting on One-Dimensional Nanopatterned

- Surfaces. *Nano Letters* **2008**, 8, 2819-2824.
- Xia, D.Y.; He, X.; Jiang, Y. B.; Lopez, G. P.; Brueck, S. R. J. Tailoring Anisotropic Wetting Properties on Submicrometer-Scale Periodic Grooved Surfaces. *Langmuir* **2010**, 26, 2700–2706.
- Xia, Y. and Whitesides, G. M. Extending microcontact printing as a microlithographic technique. *Langmuir* **1997**, 13, 2059-2067.
- Xiao, R., Chu, K.-H. & Wang, E. N. Multi-layer liquid spreading on superhydrophilic nanostructured surfaces. *Appl. Phys. Lett.* **2009**, 94, 193104.
- Yang, J.; Rose, F. R. A. J.; Gadegaard, N. and Alexander, M. R.; Effect of Sessile Drop Volume on the Wetting Anisotropy Observed on Grooved Surfaces. *Langmuir* **2009**, 25, 2567-2571.
- Yao, Ke Xin; Zeng, Hua Chun. Fabrication and Surface Properties of Composite Films of SAM/Pt/ZnO/SiO₂. *Langmuir* **2008**, 24, 14234–14244.
- Yoshimitsu, Z.; Nakajima, A.; Watanabe, T.; Hashimoto, K. Effects of Surface Structure on the Hydrophobicity and Sliding Behavior of Water Droplets. *Langmuir* **2002**, 18, 5818-5822.
- Young, N. O. and Kowal, J. Optically active fluorite films. *Nature (London)* **1959**. 183, 104 -105.
- Young, T. An Essay on the Cohesion of Fluids, *Philosophical Transactions of the Royal Society of London*, **1805**, 95, 65-87.
- Youngblood, J. P.; McCarthy, T. Ultrahydrophobic Polymer Surfaces Prepared by Simultaneous Ablation of Polypropylene and Sputtering of Poly(tetrafluoroethylene) Using Radio Frequency Plasma. *Macromolecules*, **1999**, 32, 6800–6806.
- Zhang, F. X. and Low, H.Y. Anisotropic Wettability on Imprinted Hierarchical Structures, *Langmuir*, **2007**, 23, 7793–7798.
- Zhang, F. X. and Low, H.Y. Ordered three-dimensional hierarchical nanostructures by nanoimprint lithography. *Nanotechnology* **2006**, 17, 1884–1890.
- Zhang, J., Cheng, Z., Zheng, Y. & Jiang, L. Ratchet-induced anisotropic behavior of superparamagnetic microdroplet. *Appl. Phys. Lett.* **2009**, 94, 144104.
- Zhao, B.; Moore, J. S.; Beebe, D. J. Surface-directed liquid flow inside microchannels. *Science (N.Y.)* **2001**, 291, 1023-1026.
- Zhao, Y.; Lu, Q. H.; Li, M.; Li, X. Anisotropic wetting characteristics on submicrometer-scale

- periodic grooved surface. *Langmuir* **2007**, 23, 6212–6217.
- Zhao, Y. P.; Ye, D. X.; Wang, P. I.; Wang, G. C.; Lu, T. M.; Fabrication Si nano-columns and square springs on self-assembly colloid substrates. *International Journal of Nanoscience*, **2002**, 1, 87-90.
- Zhao, Y. P.; Ye, D. X.; Wang, G. C.; Lu, T. M.; Novel nano-column and nano-flower arrays by glancing angle deposition. *Nano Letters* **2002**, 2, 351–354.
- Zheng, Y. M., Gao, X. F. & Jiang, L. Directional adhesion of superhydrophobic butterfly wings. *Soft Material* **2007**, 3, 178-182.

APPENDIX A

THE CALCULATION OF ARBITRARY ARC LENGTH ALONG A COSINE FUNCTION

In order to get the theoretical roughness factor of the CD surface, we need to calculate an arbitrary arc length S_{abcde} along a cosine function, as shown in the Fig. 3.4. To begin with, for any functional equation $y = f(x)$, the arbitrary arc length calculation is resorted to the integration as shown in Fig.A-1:

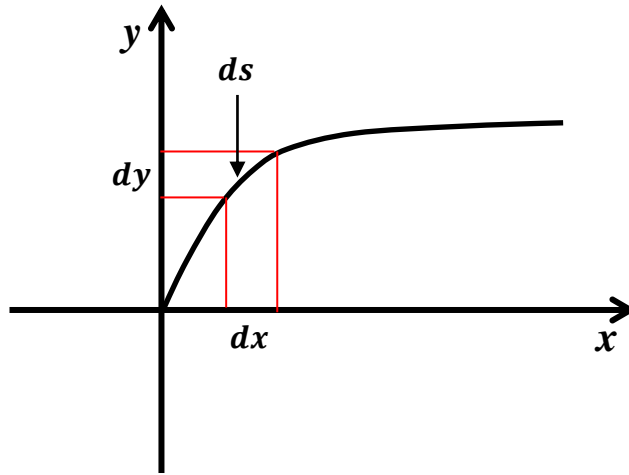


Figure A-1. A demonstration of the calculation of element of length along an arbitrary arc, where $(ds)^2 = (dx)^2 + (dy)^2$ and $dy = y' \cdot dx$.

Thus we can get the element of length:

$$ds = \sqrt{1 + (y')^2} \cdot dx. \quad (\text{A-1})$$

Specifically, as regarding our case, $y = A \cos \omega x$, where $A = 89 \text{ nm}$, $\omega = 2\pi/\lambda$ and $\lambda = 1429 \text{ nm}$, the element of length can be expressed as,

$$ds = \sqrt{1 + (y')^2} \cdot dx = \sqrt{1 + (-A\omega \sin \omega x)^2} \cdot dx. \quad (\text{A-2})$$

Consequently, the arc length from a to b in Fig.3.2 can be expressed as,

$$S_{ab} = S_{ab} = \int_0^{\frac{\lambda}{4}} \sqrt{(1 + (-A\omega \sin \omega x)^2)} \cdot dx. \quad (\text{A-3})$$

and
$$S_{abcde} = 4 \cdot S_{ab} = 4 \int_0^{\frac{\lambda}{4}} \sqrt{(1 + (-A\omega \sin \omega x)^2)} \cdot dx. \quad (\text{A-4})$$

This calculation is very hard to be solved out manually due to the complex integral calculation problem. However, a MATLAB program was written to implement the computation and the obtained results S_{abcde} is equal to 1482 nm.

Following is the code for MATLAB Programming:

```
clear all;
clc;
syms x;
A = 89;
T = 1429;
w = 2*pi/T;
v=int(sqrt(1+((A*w)*sin(w*x))^2),x,0,T/4);
S_ab = double(v);
S_abcde = 4*S_ab;
```

APPENDIX B

FREE ENERGY AND FREE ENERGY BARRIER DISTRIBUTION ON GROOVED SURFACE

In order to better understand the physics of this anisotropic wetting and three-phase contact lines contortion on our engineered samples surface, a thermodynamic model based on the calculations of the free energy barrier (FEB) as a function of measureable surface morphology parameters along the surface grooves was developed, as it can be seen in the figure 3.9. It is believed that this analysis could be used to reveal the thermodynamic mechanism for the anisotropic wetting behavior and the formation of the watermark.

Before we introduce the proposed thermodynamic model in detail, we would like to provide insight to the concept of free energy barrier (FEB), which is critical to the interpretation of our anisotropic wetting. For a system with a liquid drop sitting on a solid surface, the free energy barrier is considered to be the energy needed for the drop to move from a metastable state to an adjacent one. More specifically, the free energy barrier refers to the free energy difference between a local minimum and an adjacent maximum in the direction of three-phase line motion (i.e. advancing or receding), which is directly related to the free energy change of the system.

All our engineered samples are fabricated based on the CD grooved structure. And this groove texture dominated all the engineered samples surface morphology. And, what is more, the periodicity of the groove structure holds consistent through all the samples. The sketches for all the possible surface morphologies of our engineered samples can be found in Figure B-1.

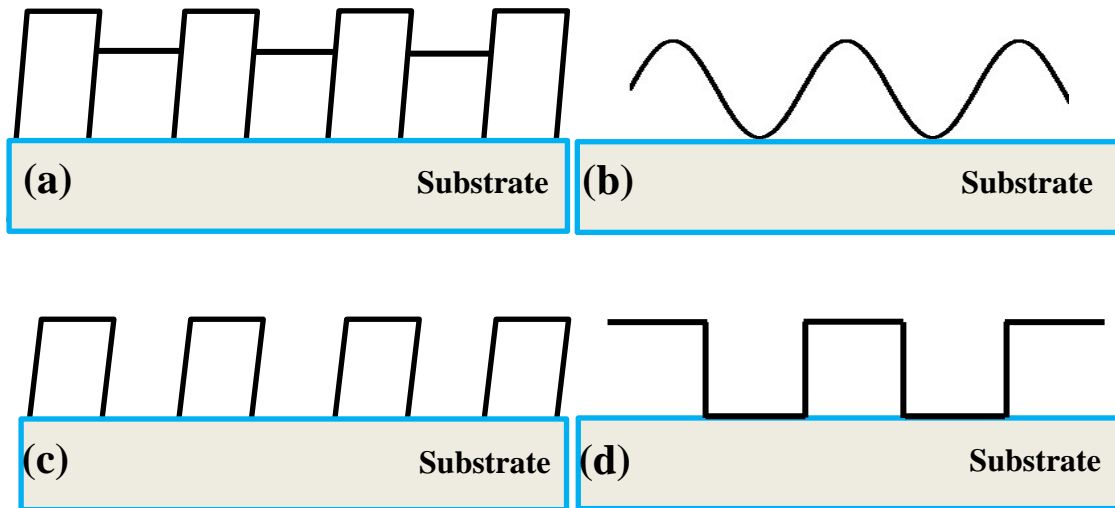


Figure B-1. Sketches for cross-sectional view of all the possible surface morphologies of our engineered samples. (a) SiNR on CD substrate with parallel growth. (b) Polymer-stripped-off CD surface, if we assume the surface morphology is cosinoidal or sinusoidal. (c) SiNR on CD substrate with vertical growth. (d) Polymer-stripped-off CD surface, if we assume the surface morphology is rectangular. However, no matter what the surface morphology is, all the water droplets are resting in a *hemi-wicking* state.

Based on the sketches showing in Fig. B-1., it is reasonable for us to take the groove texture in a rectangular shape as the typical surface morphology to calculate the free energy barrier (FEB) as a function of measurable surface morphology parameters. And also, the same analysis could be easily extended to any other kinds of groove texture.

In principle, based on the minimization of surface free energy of a system formed between a 3-dimensional surface structure and a water drop, thermodynamically stable and metastable states could be found, and the corresponding surface geometrical configurations that lead to the desired stable and metastable states with free energy barrier (FEB) can be calculated. Following are the basic assumptions of the thermodynamic model for the FEB calculation.

- a. The water droplet on the sample surface is in a Wenzel's state, and the water will penetrate and fill up the troughs between the grooves.
- b. The cross-sectional view of water drop profile is spherical and the drop size is much larger than the groove size (parameters a , b and h in figure 3.9). This assumption is

well satisfied, because the droplet file is usually in a millimeter scale, however, the surface morphology parameter is in a nano/sub-nanometer scale.

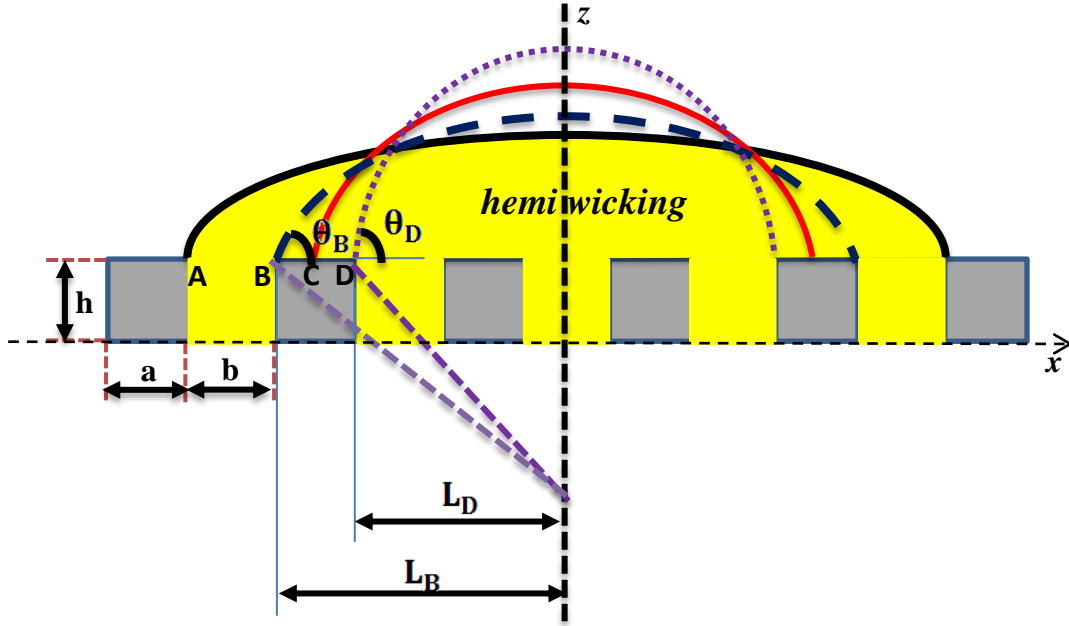


Figure B-2. A cross-sectional view of the model of the groove texture. For all the samples, when we deposit a water droplet onto the samples, the liquid will escape from the droplet and penetrate into the troughs between the grooves, and the water droplet will rest in a *hemi-wicking* state.

Given the basic sketch in Fig.B-1, we can easily get the roughness factor in Wenzel's Law ($r = a + b + 2h/a + b$) and the solid fraction in Cassie's Law ($f = a/a + b$). Here we further assume that the three phase contact line can only rest on the edge of the grooves, such as the resting point A, B, D, and cannot rest on the point C in Fig.B-2 (Johnson and Dettre, 1964; Li and Amirfazli, 2005).

These states are metastable because the interfacial tension would tend to move the drop back to these states, if the external causes(vibration, air currents, evaporation or inverted syringe imbibition) is not large enough to overcome the free energy barrier (FEB). For each metastable state A, B, D, it is associated with a free energy and an apparent contact angle: $\theta_A, \theta_B, \theta_D$, respectively.

First, let us consider the case when the drop recedes from position B to position D, and the magnitude of free energy per unit length of drop perpendicular to $y = 0$ plane for each of the two cases can be written as:

$$E_B = \gamma_{la} l_B^{la} + \gamma_{ls} l_B^{ls} + E_o, \quad (\text{B-1})$$

$$E_D = \gamma_{la} l_D^{la} + \gamma_{sa} l_D^{sa} + E_o, \quad (\text{B-2})$$

where E_o is part of the free energy of the system that remains unchanged as a result of the three-phase contact line receding from metastable state B to its adjacent metastable state D. In the sector, which is consisted of the liquid-air contact line of the droplet, radius R of this curvature and the medial axis z , we can obtain that $l^{la} = \theta \cdot R = \theta \cdot L / \sin \theta$ and $l_B^{ls} = l_D^{sa} = a$, where L denotes the drop width, a is the width of the ridge, b and h are the width and the depth of the grooves, respectively.

For the model indicated in Fig.B-2, geometrically, the drop area is constant in the x - z plane when the three phase contact line receding from B to D, due to the constant drop volume. And the geometric equation for a constant cross sectional area can be written as:

$$\theta_D \frac{L_D^2}{(\sin \theta_D)^2} - L_D^2 \cot \theta_D = \theta_B \frac{L_B^2}{(\sin \theta_B)^2} - L_B^2 \cot \theta_B, \quad (\text{B-3})$$

$$\text{and} \quad L_B = L_D + a. \quad (\text{B-4})$$

Furthermore, the Young's equation is locally valid respectively when the droplet rest in the metastable state B and D, thus the Young' equation can be written as:

$$\gamma_B^{la} \cdot \cos \theta_B = \gamma_B^{sa} - \gamma_B^{ls}, \quad (\text{B-5})$$

$$\gamma_D^{la} \cdot \cos \theta_D = \gamma_D^{sa} - \gamma_D^{ls}, \quad (\text{B-6})$$

where $\gamma_B^{la} = \gamma_D^{la}$ for a same water droplet and $\theta_B = \theta_D$, which is the Young's contact angle, in our case $\theta_B = \theta_D = \theta_{Si} = 28 \pm 1^\circ$.

The free energy barrier in this receding processing is :

$$\nabla E_R = E_D - E_B. \quad (\text{B-7})$$

Submit the equation B-1 and B-2 into the equation B-7, and then combine the equation B-5 and B-6, we can finally get the free energy barrier (FEB) in the receding processing from metastable state B to its adjacent metastable state D:

$$\nabla E_R = \gamma_{la} \left(\theta_D \frac{L_D}{\sin \theta_D} - \theta_B \frac{L_B}{\sin \theta_B} \right) + \gamma_{la} \cdot a \cdot \cos \theta_{Si}. \quad (\text{B-8})$$

Take the sample of SiNR on CD surface with vertical growth for an example, we can get the parameters $\gamma_{la} = 72.6 \text{ mN/m}$, $L_B = 2.62 \times 10^{-3} \text{ m}$, $a = 0.423 \times 10^{-6} \text{ m}$, $b = 1.006 \times 10^{-6} \text{ m}$, $h = 1.172 \times 10^{-6} \text{ m}$.

For various contact angle value of θ_B in the range of possible CA between advancing and receding, and also corresponding θ_D confine by the equation B-3 and B-4, the free energy barrier (FEB) could be calculated, as it can be seen in the Fig.B-3.

Likewise, we could also calculate the free energy barrier (FEB) needed to be overcome, when the three-phase contact line advances from metastable state B to its adjacent metastable state A, as it can be seen in Fig.B-2.

In the processing of three-phase contact line advancing from state B to state A, the geometric equation for a constant cross sectional area can be written as:

$$\theta_B \frac{L_B^2}{(\sin \theta_B)^2} - L_B^2 \cot \theta_B = \theta_A \frac{L_A^2}{(\sin \theta_A)^2} - L_A^2 \cot \theta_A + 2bh, \quad (\text{B-9})$$

$$L_A = L_B + a. \quad (\text{B-10})$$

We can get the free energy barrier (FEB) in the advancing processing from metastable state B to its adjacent metastable state A as following:

$$\nabla E_A = \gamma_{la} \left(\theta_A \frac{L_A}{\sin \theta_A} - \theta_B \frac{L_B}{\sin \theta_B} \right) - \gamma_{la} \cdot (b + 2h) \cdot \cos \theta_{Si}. \quad (\text{B-11})$$

Then, the free energy barrier (FEB) distribution, when the three-phase contact line advances from metastable state B to its adjacent metastable state A, can also be seen in Fig.B-3.

From the Fig.B-3, we can see that there are a lot of free energy barriers (FEB) in the direction of perpendicular to the groove surface. And the anisotropic geometry allows the liquid drop to preferentially spread along the groove rather than perpendicularly due to the higher energy required to overcome the energy barriers between metastable states. Perpendicularly to the surface grooves, no matter the three-phase contact line advances from metastable state B to its adjacent metastable state A, or recedes from metastable state B to its adjacent metastable state D, they all need to overcome the free energy barriers between metastable states. That is to say, during the process of reaching the equilibrium state after contacting the surface, the drop that is initially present in the air as a sphere has to overcome a series of energy barriers caused by the groove edge.

From a thermodynamic view, when the water droplet spreads on the sample surface, the parallel three phase contact line can move easily, because there are few energy barriers in the groove parallel direction. However, the perpendicular three phase contact line feels the presence of energy barriers imposed by the periodic surface groove edges, and thus it gets pinned. In the continuous water spreading processing, when the three phase contact line moves perpendicular to the grooves, reaches the neighboring groove, and gets pinned again at a position similar to that of the previous groove. Therefore, the perpendicular contact line advances in a pinning-depinning-repinning manner (de Gennes, et al. 1985; Youngblood and McCarthy, et al. 1999; Morita, et al. 2005). And the final state of the drop will stay at a metastable state at which its free surface energy is lower than its neighboring states (Long, et al. 2005).

The aforementioned thermodynamic analysis provides insight into anisotropic wetting on our engineered samples surface, especially, the water preferential spreading mechanism and also the physics beneath the contortion of the three-phase contact lines.

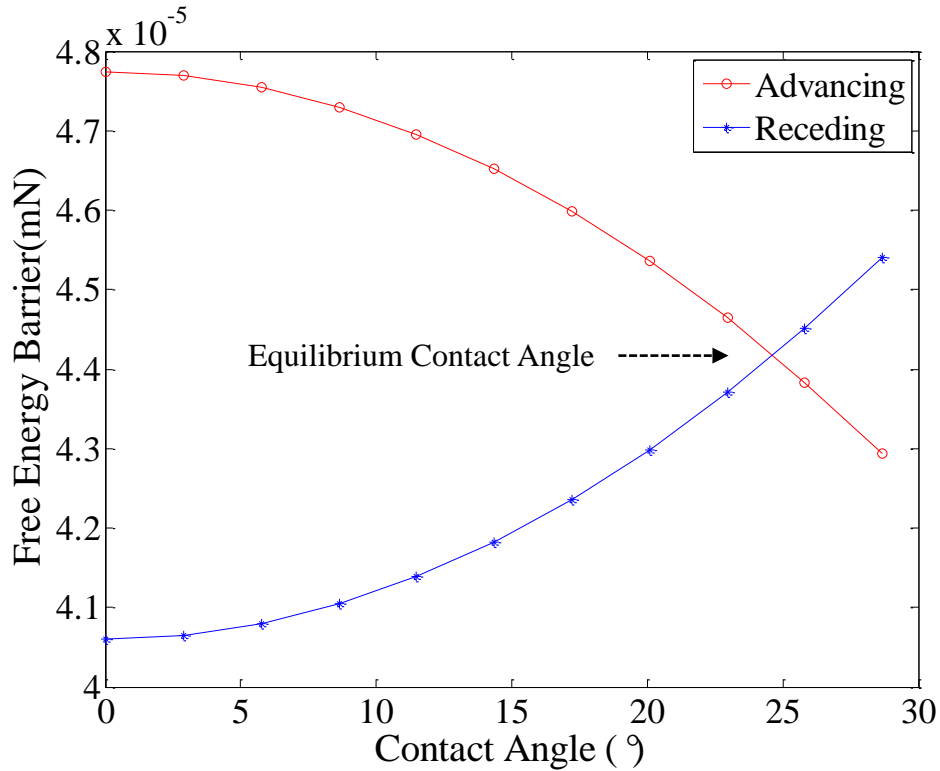


Figure B-3. Free energy barrier distribution when the water spreads perpendicularly to the surface grooves for a noncomposite wetting state. Here, the equilibrium contact angle is 24.6° , which is consistent with our experimental results $\theta_{\text{Si-CD-X}} = 25 \pm 3^\circ$ (CCD || Groove).

Understandably, the water droplet will easily and preferentially spread along the groove rather than perpendicularly. And thus, macroscopically, we can observe the watermarks and droplets are in a shape of such as ellipse, elongated and parallel-sided, or belt-like shape.

APPENDIX C

SLIDING ANGLE QUALITATIVE ANALYSIS IN A THERMODYNAMIC VIEW

Tilting our samples to a critical angle θ_s relative to the horizontal imparts a downslope gravitational force of magnitude $F_g = mg \sin \theta_s$ on the droplet, where $mg = \rho gV$ and ρ is the density of the water, g is the gravitational acceleration and V is the droplet volume, in our case, which is fixed at $10\mu\text{l}$.

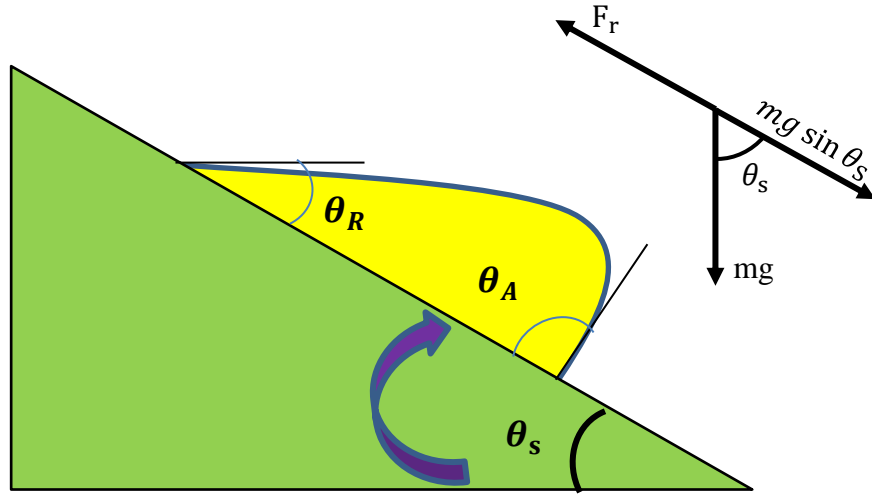


Figure C-1. Sketch with force analysis of the sliding angle captured by tilting base method. At a critical angle θ_s , the water droplet begins to roll off the substrate surface.

At this critical point with a sliding angle θ_s , the droplet is on the verge of motion, there is a net retention force F_r opposes and offset the component force $mg \sin \theta_s$, as we can get:

$$F_r = F_g = mg \cdot \sin \theta_s = \rho gV \cdot \sin \theta_s. \quad (\text{C-1})$$

As regarding the retention force, Dussan (Dussan, 1985) and Furmidge (Furmidge, 1962), showed that the retention force, F_r , obeys

$$F_r = w\gamma(\cos \theta_R - \cos \theta_A). \quad (\text{C-2})$$

where w is the width of the water droplet, γ is the liquid surface tension, θ_R and θ_A are the receding and advancing contact angle, respectively.

Particularly, Dussan (Dussan, 1985) showed that for small contact angle hysteresis one can write equation C-2 as:

$$F_r = \gamma V^{1/3} \left(\frac{96}{\pi}\right)^{1/3} (\cos \theta_R - \cos \theta_A) \left[\frac{(1 + \cos \theta_A)^{3/4} \left(1 - \frac{3}{2} \cos \theta_A + \frac{1}{2} \cos \theta_A^3\right)}{(\cos \theta_A + 2)^{3/2} (1 - \cos \theta_A)^{9/4}} \right]^{2/3} \quad (C-3)$$

Submit the equation C-1 into the equation C-2, we can get that:

$$\sin \theta_s = \frac{\gamma}{\rho g V^{2/3}} \left(\frac{96}{\pi}\right)^{1/3} (\cos \theta_R - \cos \theta_A) \left[\frac{(1 + \cos \theta_A)^{3/4} \left(1 - \frac{3}{2} \cos \theta_A + \frac{1}{2} \cos \theta_A^3\right)}{(\cos \theta_A + 2)^{3/2} (1 - \cos \theta_A)^{9/4}} \right]^{2/3} \quad (C-4)$$

From the equation C-2 and C-4 , we can safely conclude that the sliding angle is determined by several factors, including the surface tension, density of the liquid, volume of the testing droplet, contact angle hysteresis, gravitational acceleration. Specifically, the sliding angle is proportional to the surface tension of the testing liquids, and contact angle hysteresis, inversely proportional to the liquid density, droplet volume and gravitational acceleration.

Based on the theory of Dussan about sliding angle, in our case, all the aforementioned factors related to the sliding angle except for the contact angle hysteresis are fixed. Consequently, before the interpretation of our sliding angle on the Silicon nanorods modified surface, we may want to do some investigation about the contact angle hysteresis on the titled nanorods surface.

Malvadkar (Malvadkar, et al. 2010) studied the contact angle hysteresis on the titled nanorods from two direction: one is pin direction and another is release direction. Specifically, pin direction means the substrate titled direction is same as the vapor incident direction. In this

case, the surface morphology anisotropy leads to the pin behavior relative to the orientation of the nanorods. That is to say, the three phase contact line was pinned by the tilted nanorods when it move forwards. Malvadkar (Malvadkar, et al. 2010) quantitatively showed us that the advancing and receding contact angle can be expressed as following in this pin direction:

Advancing contact angle in the pin direction:

$$\theta_{A-PIN} = \lambda \min(\pi, \theta_{a0} + \beta) + (1 - \lambda)\pi. \quad (C-5)$$

Receding contact angle in the pin direction:

$$\theta_{R-PIN} = \lambda(\theta_{a0} - \beta) + (1 - \lambda)\pi. \quad (C-6)$$

And Malvadkar (Malvadkar, et al. 2010) also pointed out that in the release direction, which is the direction when the substrate tilted direction is opposite to the vapor incident direction, the advancing and receding contact angle could be written as:

Advancing contact angle in the release direction:

$$\theta_{A-REL} = \lambda \min(\pi, \max(\theta_{a1}, \theta_{a2})) + (1 - \lambda)\pi. \quad (C-7)$$

where $\theta_{a1} = 3\pi/2 - \beta - \arctan(\cot(\beta)/(1 - s))$ and $\theta_{a2} = \theta_{a0} + \pi/2 - \beta$.

Receding contact angle in the release direction:

$$\theta_{R-REL} = \lambda(\theta_{r0} + \beta - \pi/2) + (1 - \lambda)\pi. \quad (C-8)$$

For the equation C-4 to C-8, θ_{a0} and θ_{r0} are the intrinsic advancing and receding contact angle of a flat surface of the material. β is the nanorods tilted angle, d is the nanorod diameter, δ is the nanorods perpendicular spacing, and s is the solid fraction in the longitudinal direction as $s = d/\delta$. In addition, λ is the linear fraction of the advancing or receding contact line on the nanorods, which is approximately equal to $\pi s / (2(1 + (\pi/2 - 1)s))$.

Based on the above equations and corresponding analysis, we can see that, as regarding of the surface of tilted nanorods, we have larger contact angle hysteresis in the pin direction,,

compared with the contact angle hysteresis in the release direction. Consequently, based on the relationship between the sliding angle and contact angle hysteresis from equation C-1 and C-3, we should have larger sliding angle in the pin direction.

This is well consistent with our experimental results. For the sample of silicon nanorods modified silicon wafer, we have sliding angle $77\pm 4^\circ$ in the pin direction, and $46\pm 1^\circ$ in the release direction. For the sample of silicon nanorod parallel growth on CD substrate, we have sliding angle $71\pm 7^\circ$ in the pin direction, and $34\pm 3^\circ$ in the release direction. Likewise, as regarding the sample of silicon nanorods vertical growth on the CD substrate, we also have the sliding angle $49\pm 2^\circ$ in the pin direction and $23\pm 1^\circ$ in the release direction.